CEERS: 7.7 μm PAH Star Formation Rate Calibration with JWST MIRI

Kaila Ronayne, Casey Papovich, Guang Yang, Lu Shen, Mark Dickinson, Robert Kennicutt, Anahita Alavi, Pablo Arrabal Haro, Micaela B. Bagley, Denis Burgarella, et al.

The Astrophysical Journal, 970:61 (16pp), 2024 July 20 https://doi.org/10.3847/1538-4357/ad5006

CEERS: 7.7 μm PAH Star Formation Rate Calibration with JWST MIRI

Kaila Ronayne[1,2], Casey Papovich[1,2], Guang Yang[3,4], Lu Shen[1,2], Mark Dickinson[5], Robert Kennicutt[1,2,6], Anahita Alavi[7], Pablo Arrabal Haro[5], Micaela B. Bagley[8], Denis Burgarella[9], Aurélien Le Bail[10], Eric F. Bell[11], Nikko J. Cleri[1,2], Justin Cole[1,2], Luca Costantin[12], Alexander de la Vega[13], Emanuele Daddi[10], David Elbaz[10], Steven L. Finkelstein[8], Norman A. Grogin[14], Benne W. Holwerda[15], Jeyhan S. Kartaltepe[16], Allison Kirkpatrick[17], Anton M. Koekemoer[18], Ray A. Lucas[18], Benjamin Magnelli[10], Bahram Mobasher[13], Pablo G. Pérez-González[12], Laura Prichard[14], Marc Rafelski[18,19], Giulia Rodighiero[20,21], Ben Sunnquist[18], Harry I. Teplitz[7], Xin Wang[22], Rogier A. Windhorst[23], and L. Y. Aaron Yung[24,25]

[1] Department of Physics and Astronomy, Texas A&M University, College Station, TX 77843-4242, USA
[2] George P. and Cynthia Woods Mitchell Institute for Fundamental Physics and Astronomy, Texas A&M University, College Station, TX 77843-4242, USA
[3] Kapteyn Astronomical Institute, University of Groningen, P.O. Box 800, 9700 AV Groningen, The Netherlands
[4] SRON Netherlands Institute for Space Research, Postbus 800, 9700 AV Groningen, The Netherlands
[5] NSF's National Optical-Infrared Astronomy Research Laboratory, 950 N. Cherry Ave., Tucson, AZ 85719, USA
[6] Department of Astronomy and Steward Observatory, University of Arizona, Tucson, AZ 85721, USA
[7] IPAC, California Institute of Technology, 1200 E. California Blvd., Pasadena, CA 91125, USA
[8] Department of Astronomy, The University of Texas at Austin, Austin, TX, USA
[9] Aix Marseille Univ, CNRS, CNES, LAM Marseille, France
[10] Université Paris-Saclay, Université Paris Cité, CEA, CNRS, AIM, 91191, Gif-sur-Yvette, France
[11] Department of Astronomy, University of Michigan, 1085 S. University Ave., Ann Arbor, MI 48109-1107, USA
[12] Centro de Astrobiología (CAB), CSIC-INTA, Ctra de Ajalvir km 4, Torrejón de Ardoz, 28850, Madrid, Spain
[13] Department of Physics and Astronomy, University of California, 900 University Ave., Riverside, CA 92521, USA
[14] Space Telescope Science Institute, Baltimore, MD, USA
[15] Physics & Astronomy Department, University of Louisville, Louisville, KY 40292, USA
[16] Laboratory for Multiwavelength Astrophysics, School of Physics and Astronomy, Rochester Institute of Technology, 84 Lomb Memorial Dr., Rochester, NY 14623, USA
[17] Department of Physics and Astronomy, University of Kansas, Lawrence, KS 66045, USA
[18] Space Telescope Science Institute, 3700 San Martin Dr., Baltimore, MD 21218, USA
[19] Department of Physics and Astronomy, Johns Hopkins University, Baltimore, MD 21218, USA
[20] Department of Physics and Astronomy, Università degli Studi di Padova, Vicolo dell'Osservatorio 3, I-35122, Padova, Italy
[21] INAF—Osservatorio Astronomico di Padova, Vicolo dell'Osservatorio 5, I-35122, Padova, Italy
[22] School of Astronomy and Space Sciences, University of the Chinese Academy of Sciences (UCAS), Beijing 100049, People's Republic of China
[23] School of Earth and Space Exploration, Arizona State University, Tempe, AZ 85287-1404, USA
[24] Astrophysics Science Division, NASA Goddard Space Flight Center, 8800 Greenbelt Rd., Greenbelt, MD 20771, USA
Received 2023 October 11; revised 2024 April 30; accepted 2024 May 14; published 2024 July 17

Abstract

We test the relationship between UV-derived star formation rates (SFRs) and the 7.7 μm polycyclic aromatic hydrocarbon luminosities from the integrated emission of galaxies at $z \sim 0$–2. We utilize multiband photometry covering 0.2–160 μm from the Hubble Space Telescope, CFHT, JWST, Spitzer, and Herschel for galaxies in the Cosmic Evolution Early Release Science (CEERS) Survey. We perform spectral energy distribution (SED) modeling of these data to measure dust-corrected far-UV (FUV) luminosities, $L_{\rm FUV}$, and UV-derived SFRs. We then fit SED models to the JWST/MIRI 7.7–21 μm CEERS data to derive rest-frame 7.7 μm luminosities, L_{770}, using the average flux density in the rest-frame MIRI F770W bandpass. We observe a correlation between L_{770} and $L_{\rm FUV}$, where $\log L_{770} \propto (1.27 \pm 0.04) \log L_{\rm FUV}$. L_{770} diverges from this relation for galaxies at lower metallicities, lower dust obscuration, and for galaxies dominated by evolved stellar populations. We derive a "single-wavelength" SFR calibration for L_{770} that has a scatter from model estimated SFRs ($\sigma_{\Delta \rm SFR}$) of 0.24 dex. We derive a "multiwavelength" calibration for the linear combination of the observed FUV luminosity (uncorrected for dust) and the rest-frame 7.7 μm luminosity, which has a scatter of $\sigma_{\Delta \rm SFR} = 0.21$ dex. The relatively small decrease in σ suggests this is near the systematic accuracy of the total SFRs using either calibration. These results demonstrate that the rest-frame 7.7 μm emission constrained by JWST/MIRI is a tracer of the SFR for distant galaxies to this accuracy, provided the galaxies are dominated by star formation with moderate-to-high levels of attenuation and metallicity.

Unified Astronomy Thesaurus concepts: Star formation (1569); Polycyclic aromatic hydrocarbons (1280); James Webb Space Telescope (2291); Hubble Space Telescope (761); Galaxy evolution (594); Infrared galaxies (790)

1. Introduction

Measuring the rate at which galaxies form stars (the star formation rate, SFR) remains a challenge in astrophysics. SFRs are not measured directly, but rather estimated based on observations of the direct or reprocessed light produced by young stars. In turn this estimation is extrapolated to a total

[25] NASA Postdoctoral Fellow.

SFR based on assumptions of the stellar initial mass function (IMF; see reviews by Kennicutt 1998; Kennicutt & Evans 2012). There have been a number of empirically derived SFR calibrations making use of the continuum or emission lines that have been demonstrated to be indicative of the short-lived stellar populations in galaxies (e.g., Calzetti et al. 2007; Houck et al. 2007; Hernán-Caballero et al. 2009; Kennicutt et al. 2009; Hao et al. 2011; Shipley et al. 2016; Xie & Ho 2019; Cleri et al. 2022). Such tracers of star formation range from the X-ray to the radio, and exhibit varying ability to estimate SFRs without large uncertainties (with calibration systematics on the order of 30%; Kennicutt 1998), where at least some of this is contingent upon the properties of a galaxy (e.g., stellar mass, optical depth, etc.; Kennicutt & Evans 2012). Understanding the galaxy properties that limit the accuracy of SFR tracers is crucial. Frequently employed SFR tracers such as Hα, far-UV (FUV), near-UV (NUV), and even the widely recognized Paα suffer from attenuation by dust (Calzetti et al. 1994; Papovich et al. 2009), which can reduce the certainty of SFR estimates when employed for dust-obscured galaxies (Kennicutt 1998).

Another complication is that most of the stellar light from galaxies at cosmic noon is absorbed and then emitted again at longer wavelengths, where obscured galaxies contribute up to ~80% of the star-forming population for $z \sim 1$–3 (Madau & Dickinson 2014). As such, calibrations for tracers that are capable of measuring SFRs for obscured galaxies are essential for discerning the overall picture of star formation during these epochs. The infrared (IR) has been frequently employed for this purpose in the obscured population of galaxies, more specifically the total-IR luminosity ($L_{\rm TIR} = 3$–$1100\ \mu$m; Hao et al. 2011), the mid-IR polycyclic aromatic hydrocarbons (PAHs; Shipley et al. 2016), and the 24 μm emission (Rieke et al. 2009). Tracers that rely on far-IR data have not been the subject of many recent studies since the end of far-IR space-based missions such as Spitzer, Herschel, the Infrared Astronomical Satellite, and the Infrared Space Observatory. As JWST (Gardner et al. 2006) continues to unveil new dust-obscured galaxies, there is a growing need for new methods to study star formation.

The mid-IR offers new opportunities to explore star formation in dust-obscured galaxies, which is imperative for understanding the new era of galaxies uncovered with JWST. The mid-IR covers strong PAH emission features at rest-frame wavelengths 3–18 μm, which are found in photo-dissociation regions surrounding H II regions (Calzetti et al. 2007; Smith et al. 2007). PAHs contribute up to 20% of the total-IR luminosity for star-forming galaxies (Elbaz et al. 2011), with the 7.7 μm feature consisting of up to half of the total PAH luminosity (Smith et al. 2007). The 7.7 μm PAH emission has been shown in previous works to correlate with the SFR for resolved star-forming regions (Calzetti et al. 2007) and for the integrated emission of galaxies (Houck et al. 2007; Pope et al. 2008, 2013; Hernán-Caballero et al. 2009; Cluver et al. 2014; Shipley et al. 2016; Xie & Ho 2019). However, the correlation between the PAH emission and the SFR at $z > 1$ for large samples remains an unexplored territory in literature due to the sensitivity of available IR instruments prior to the launch of JWST.

The JWST mid-IR instrument (MIRI; Wright et al. 2023) is sensitive to the emission from galaxies at wavelengths ~5–28 μm, including those from the PAH features at an unprecedented level. Results from the first year of JWST highlight the capability of MIRI to trace the PAH features and constrain the 7.7 μm PAH emission (e.g., Chastenet et al. 2023; Evans et al. 2022; Yang et al. 2023b; Dale et al. 2023; Kirkpatrick et al. 2023; Shen et al. 2023). The 7.7 μm emission can be observed up to a redshift of 2 with the available MIRI bands, and can achieve depths of up to two orders of magnitude fainter than Spitzer. There have yet to be galaxy-scale star formation (SF) studies done for the 7.7 μm emission with MIRI, with the exception of preliminary tests from Battisti et al. (2015), Senarath et al. (2018), Shipley et al. (2016), McKinney et al. (2020), and Kirkpatrick et al. (2023). MIRI observations allow us to probe the faint end of the relation between the 7.7 μm feature and SFR that has yet to be observed by any of the JWST predecessors out to $z \sim 2$.

This paper presents one of the first tests of the rest-frame 7.7 μm PAH emission using JWST/MIRI imaging to track the SFR on galaxy-wide scales for sources at redshifts 0–2. To do this, we perform spectral energy distribution (SED) modeling with multiband photometry from the UV to far-IR in addition to MIRI photometry from the Cosmic Evolution Early Release Science (CEERS) survey (Finkelstein et al. 2017; Yang et al. 2023b). We use the model SEDs to measure the rest-frame observed FUV luminosity (uncorrected for dust), FUV attenuation (A(FUV)), stellar mass, and SFR. In addition, we perform SED modeling of the CEERS JWST/MIRI 7.7–21 μm data to measure the rest-frame 7.7 μm luminosity using the average flux density in the MIRI F770W bandpass (L_{770}). We compare the correlation between the dust-corrected FUV luminosity and L_{770}, and use the relation to derive a "single-wavelength" SFR calibration. We then model the dust-corrected FUV luminosity using a linear combination of the observed FUV luminosity and L_{770} for a "multiwavelength" SFR calibration.

The outline of this paper is as follows. Section 2 provides an overview of our UV, optical, mid-IR, and far-IR imaging and multiwavelength catalogs. We describe our selection methods and sample in Section 3. Section 4 describes our SED modeling and measurements of the rest- frame L_{770} and observed FUV luminosities, as well as our prescription for attenuation. In Section 5 we show our results and discuss their implications in addition to caveats in Section 6. Lastly, our summary and main conclusions are in Section 7. Throughout this paper all magnitudes are presented in the AB system (Oke & Gunn 1983; Fukugita et al. 1996). We use the standard Lambda cold dark matter (ΛCDM) cosmology with $H_0 = 70\ {\rm km\ Mpc^{-1}\ s^{-1}}$, $\Omega_\Lambda = 0.70$, and $\Omega_M = 0.30$.

2. Data

2.1. The CEERS Survey

CEERS (Finkelstein et al. 2017, 2023; proposal ID #1345) covers ~100 sq. arcmin with JWST imaging and spectroscopy, targeting the Extended Groth Strip (EGS; Davis et al. 2007). The 2022 June observations include four MIRI and NIRCam pointings taken in parallel. Pointings CEERS MIRI 1 and CEERS MIRI 2 used for this work have no overlap with the CEERS NIRCam imaging, and were covered with MIRI in six contiguous filters: F770W, F1000W, F1280W, F1500W, F1800W, and F2100W (see Bagley et al. 2023 and Yang et al. 2023b). Importantly, these two fields have overlap with the Cosmic Assembly Near-infrared Deep Extragalactic Legacy

Survey (CANDELS; Faber 2011; Grogin et al. 2011; Koekemoer et al. 2011), and they are the only two such CEERS MIRI fields that have follow-up UV imaging from Hubble Space Telescope (HST) as part of the UVCANDELS program (Wang et al. 2020; Teplitz et al. 2022). This provides coverage from 0.2 to 1.8 μm with HST-quality angular resolution, which is well matched to MIRI (see below). The other two CEERS MIRI pointings (3 and 6) observed deeply with the F560W and F770W to study the stellar populations of more distant galaxies ($z > 4$; Papovich et al. 2023) and only trace the 7.7 μm PAH emission for very low-redshift galaxies.

2.1.1. CEERS MIRI Imaging and Photometry Catalog

A full description of the MIRI data and reduction is provided in Yang et al. (2023b) but will briefly be described here (also see Yang et al. 2021, 2023a; Kirkpatrick et al. 2023; Shen et al. 2023).

The MIRI images were processed with the JWST CALIBRATION PIPELINE (v1.10.2; Bushouse et al. 2023) primarily using the default parameters for stages 1 and 2. The background was modeled with the median of all images in the same bandpass but different fields and/or dither positions. With the background subtracted from each image, the astrometry is corrected by matching to CANDELS imaging (as described in more detail in Bagley et al. 2023) prior to stage 3 processing in the pipeline. This results in the final science images, weight maps, and uncertainty images with a pixel scale of $0\farcs09\,\mathrm{pix}^{-1}$ registered to the CANDELS v1.9 WFC3 images. This last step is important as we use MIRI fluxes matched to the existing CANDELS HST catalogs.

The MIRI photometry is measured using the description provided in Yang et al. (2023b). To summarize those steps, sources are taken from the CANDELS WFC3 catalog (Stefanon et al. 2017, and see below) with T-PHOT (v2.0, Merlin et al. 2016). T-PHOT uses priors from the HST/WFC3 F160W for the lower-resolution MIRI images for the photometric analysis. The point-spread function (PSF) for each MIRI band is constructed using WEBBPSF (v1.1.1; Perrin et al. 2012). The kernels are then constructed to match the PSF from the CANDELS/WFC3 F160W image (FWHM $\simeq 0\farcs2$) to the MIRI images (FWHM $\simeq 0\farcs2$–$0\farcs5$) to extract source photometry with T-PHOT. To estimate uncertainties on object fluxes, an rms map was constructed for each MIRI mosaic to account for pixel-correlated noise. The fluxes from T-PHOT and their uncertainties estimated with these rms maps for each source are used as the MIRI catalog (see Yang et al. 2023b for more details). We note that the MIRI flux calibration has since been updated from Yang et al. (2023b) where the median offset in MIRI F770W is 0.18 mag and is substantially lower for the redder MIRI bands, which are impacted by only a few percent .[26]

2.2. CANDELS Imaging and Multiwavelength Photometry Catalog

We use the catalog from Stefanon et al. (2017), which provides matched-aperture photometry and their uncertainties for a larger range of observations covering 0.4–8 μm in the EGS field built upon the CANDELS, All-wavelength Extended Groth strip International Survey (AEGIS), and 3D-HST program with imaging from Canada–France–Hawaii Telescope (CFHT)/MegaCam, NEWFIRM/NEWFIRM, *CFHT*/WIRCAM, HST/ACS, HST/WFC3, and Spitzer/IRAC. The catalog also includes photometric redshifts and estimated properties from SED fitting of the multiwavelength photometry, which were independently carried out by 10 different groups, each using different codes and/or SED templates including FAST (Kriek et al. 2018), HyperZ (Bolzonella et al. 2000), Le Phare (Ilbert et al. 2006), WikZ (Wiklind et al. 2008), SpeedyMC (Acquaviva et al. 2012), and other available codes (Fontana et al. 2000; Lee et al. 2010). This catalog includes the spectroscopic and photometric redshifts that will be used for this work. The spectroscopic redshifts in this catalog are from the DEEP2/DEEP3 surveys (Coil et al. 2004; Willner et al. 2006; Cooper et al. 2012; Newman et al. 2013), and the photometric redshifts are measured using the methods outlined in Dahlen et al. (2013) and Mobasher et al. (2015).

2.3. UVCANDELS Imaging

We also use the HST WFC/F275W and ACS/F435W imaging as part of the Ultraviolet Imaging of a portion of the CANDELS field from UVCANDELS, a Hubble Treasury program (GO-15647; PI: H. Teplitz). The primary UVCANDELS WFC3/F275W imaging reached $m \leqslant 27$ mag for compact galaxies (corresponding to an SFR $\sim 0.2\,M_{\odot}\,\mathrm{yr}^{-1}$) at $z = 1$, and the coordinated parallel ACS/F435W imaging reached $m \leqslant 28$ mag. A UV-optimized aperture photometry method based on optical isophotes aperture was utilized, similar to the work done on the Hubble Ultra-Deep Field UV analysis (Teplitz et al. 2013; Rafelski et al. 2015). The smaller optical apertures without degradation to the image quality allows the UV-optimized photometry method to reach the expected 5σ point-source depth of 27 mag in F275W. The UV-optimized photometry yields a factor of $\sim 1.5\times$ increase in signal-to-noise ratio (S/N) in the F275W band with a higher increase in brighter extended objects, which complement the pre-existing CANDELS multiwavelength catalog from Stefanon et al. (2017). These fluxes and their uncertainties were used for our UV catalog.

2.4. Spitzer and Herschel Far-IR Data Imaging

We also use Spitzer MIPS 24 μm and Herschel PACS 100 and 160 μm photometry with their uncertainties for the EGS field from the "super-deblended" catalog of A. Le Bail et al. (2024, in preparation, as briefly described in Le Bail et al. 2023). This catalog was developed following the methods outlined in Jin et al. (2018) and Liu et al. (2018) for COSMOS and GOODS-N respectively, where specifically the MIPS and PACS photometry were extracted by PSF fitting to prior positions of galaxies from the Stefanon et al. (2017) catalog.

3. Sample

3.1. Selection Criteria

We use as our initial sample all coordinate-matched galaxies in the UVCANDELS and MIRI catalogs in fields CEERS MIRI 1 and CEERS MIRI 2 with F160W magnitude <26.6 mag (i.e., at the 90% completeness limit; see Shen et al. 2023). We select these fields as they are the only two pointings that overlap with the UVCANDELS data with the full complement of MIRI bands from 7.7 to 21 μm. We further restrict our sample to have

[26] Please visit https://www.stsci.edu/contents/news/jwst/2023/temporal-behavior-of-the-miri-reduced-count-rate.html for more.

$z < 2$ in order to ensure that the 7.7 μm PAH feature falls within the wavelength coverage of the MIRI bands. This work utilizes spectroscopic redshifts when available from Stefanon et al. (2017) and compiled from the literature (N. Hathi 2024, private communication). After visually inspecting the faintest objects in the MIRI mosaics, we determine that robust detections are possible for objects with $S/N > 4$. We then require that objects have detections more significant than 4σ in the MIRI band in which the 7.7 μm PAH feature resides (i.e., the band that includes $(1+z) \times 7.7$ μm). On average with MIRI we detect one-third of the sources detected by HST/F160W in the redshift range $0 < z < 2$ (see Figure 1). In addition to identifying faint objects in the MIRI mosaics, we also flag galaxies that either reside on the edge of the image (where there is less exposure time) or that experience contamination from bright sources or diffraction spikes. Such galaxies are marked with `mosaicFlag` $= 1$. We then only select galaxies with `mosaicFlag` $= 0$ for this work. We also identify and remove galaxies with active galactic nuclei (AGN) in our sample by using the IRAC color selection from Donley et al. (2012).

Lastly, we apply a selection to ensure we include only actively star-forming galaxies that are along the star-forming main sequence, as defined by Whitaker et al. (2014). Using the SFR and stellar mass estimates from our modeling of the SEDs (see Section 4.1 below), we measure $\Delta\mathrm{SFR_{MS}}$ defined as $|\log(\mathrm{SFR_{MS}}) - \log(\mathrm{SFR_C})|$. $\mathrm{SFR_C}$ is the model estimated SFR from the SED fitting with CIGALE as described in Section 4.1 (the subscript "C" stands for CIGALE). $\mathrm{SFR_{MS}}$ is the value of the main-sequence SFR from Whitaker et al. (2014) at a fixed stellar mass and redshift. Through visual inspection of our sources along the star-forming main sequence (Figure 2), we determine that $\Delta\mathrm{SFR_{MS}} < 0.6$ dex is sufficient to select only star-forming galaxies in our sample (that is, we select galaxies that have an SFR within a factor of $\approx$4 of the $\mathrm{SFR_{MS}}$). This selection removes both quenching/quenched galaxies (those below $\mathrm{SFR_{MS}}$) and galaxies in a "burst" that lie above $\mathrm{SFR_{MS}}$. Starbursts can also lie within the star-forming main sequence (see Elbaz et al. 2018; Gómez-Guijarro et al. 2022), which can be diagnosed using the ratio of the total-IR luminosity and the PAH luminosity. We cannot consider such sources here as less than 1% of our sources have coverage in the far-IR (at $\sim$70–160 μm), and we defer the analysis of these objects to a future study. A summary of all our selection criteria as well as the number of galaxies in our sample is listed in Table 1.

3.2. Sample Properties

Figure 3 shows the distribution of the rest-frame 7.7 μm luminosity (L_{770}) and dust-corrected FUV luminosity (L_{FUV}; see Sections 4.1 and 4.2) as a function of redshift for the 120 galaxies in our final sample (see Table 1). The majority (87%) of galaxies in our sample reside at $z > 0.5$, and the majority (89%) have inferred L_{TIR} values above $10^9\,L_\odot$. The final sample includes a large range of dust attenuation in the visual (A_V, estimated from the CIGALE SED fits in Section 4.1), ranging from $A_V = 0.35$ to 3 mag. The MIRI data detect the mid-IR emission of galaxies at much fainter flux densities than previous instruments. For example, only 4 out of 15 galaxies in our sample at $z > 1.8$ have a Spitzer/MIPS 24 μm detection with $S/N > 4$. This is relevant because it is at this redshift where the 7.7 μm feature would have been observed by Spitzer at 24 μm. These four galaxies have an average L_{TIR} of roughly $7 \times 10^{11}\,L_\odot$, whereas at the same redshifts MIRI is sensitive to the mid-IR emission from sources down to $4 \times 10^{10}\,L_\odot$, more than an order of magnitude fainter. With increased sensitivity from MIRI, we are able to observe $\mathrm{SFR_C}$ as faint as $10^{-2}\,M_\odot\,\mathrm{yr}^{-1}$ up to $\sim 10^2\,M_\odot\,\mathrm{yr}^{-1}$. With this, our final sample encompasses a wide range of galaxies with considerably varying star-forming activity, dust obscuration, and total-IR luminosities for redshifts up to 2. We explore how different properties of our sample (e.g., mass or attenuation) impact the ability of PAH to trace SF in Section 6.

4. Methods

4.1. SED Modeling

We model the SEDs built from the multiwavelength photometry for our sample with CIGALE (Boquien et al. 2019). CIGALE uses simple stellar populations and parametric star formation histories to build composite stellar populations. The code then calculates the emission from ionized gas and thermal dust emission that is balanced based on the dust attenuation from flexible attenuation curves. The `dl2014` module used for this work considers a multicomponent dust emission based on the Draine et al. (2014) models. The first dust emission component considers heating from a single source such as a stellar population, whereas the second considers variable heating linked to star-forming regions (Boquien et al. 2019). CIGALE uses a large grid of models that is fitted to the data where the physical properties are then estimated by analyzing the likelihood distribution.

We consider two different SED modeling cases for this study where we fit the data with CIGALE. For both cases we use the same parameters as shown in Table 2 at fixed redshifts. In Case 1, we fit models to the MIRI data *only* for each object to test the capability of CIGALE to derive the rest-frame 7.7 μm luminosity. This is to ensure that the measured rest-frame 7.7 μm luminosity is not influenced by the rest of the galaxy multiwavelength SED.

In Case 2 we use all available photometry from UVCANDELS through the far-IR, which includes the MIRI data. While we include far-IR data when available, only 23 of the 120 galaxies in our sample have an $S/N > 4$ detection from MIPS 24 μm, and only one source is detected by Hershel/PACS at 160 μm. Given that CIGALE is dependent on the principle of an energy balance, the MIRI data play a significant role for the Case 2 SED fitting. We will visit the significance of the MIRI data on the Case 2 models further in Section 6.3.

We use the results from the Case 2 fits to measure (1) the observed FUV luminosity, defined by Equation (3), (2) the stellar mass, (3) the $\mathrm{SFR_C}$, and (4) the estimated FUV dust attenuation (A(FUV)). We note that $\mathrm{SFR_C}$ is the SFR averaged over the previous 10 Myr using the fitted star formation histories (we discuss this further in Appendix A).

Figure 4 shows examples of CIGALE SED fits from Case 2 for several sources in our sample in order of increasing redshift. For Case 1 and Case 2 models we use the reduced χ^2 output from CIGALE and compute the mean for our final sample, which yields 1.65 and 1.53, respectively.

4.2. SED Integration and Luminosity Calculation

We calculate the average rest-frame flux in the MIRI F770W band ($\langle F_{770} \rangle$) as an approximation for the 7.7 μm brightness.

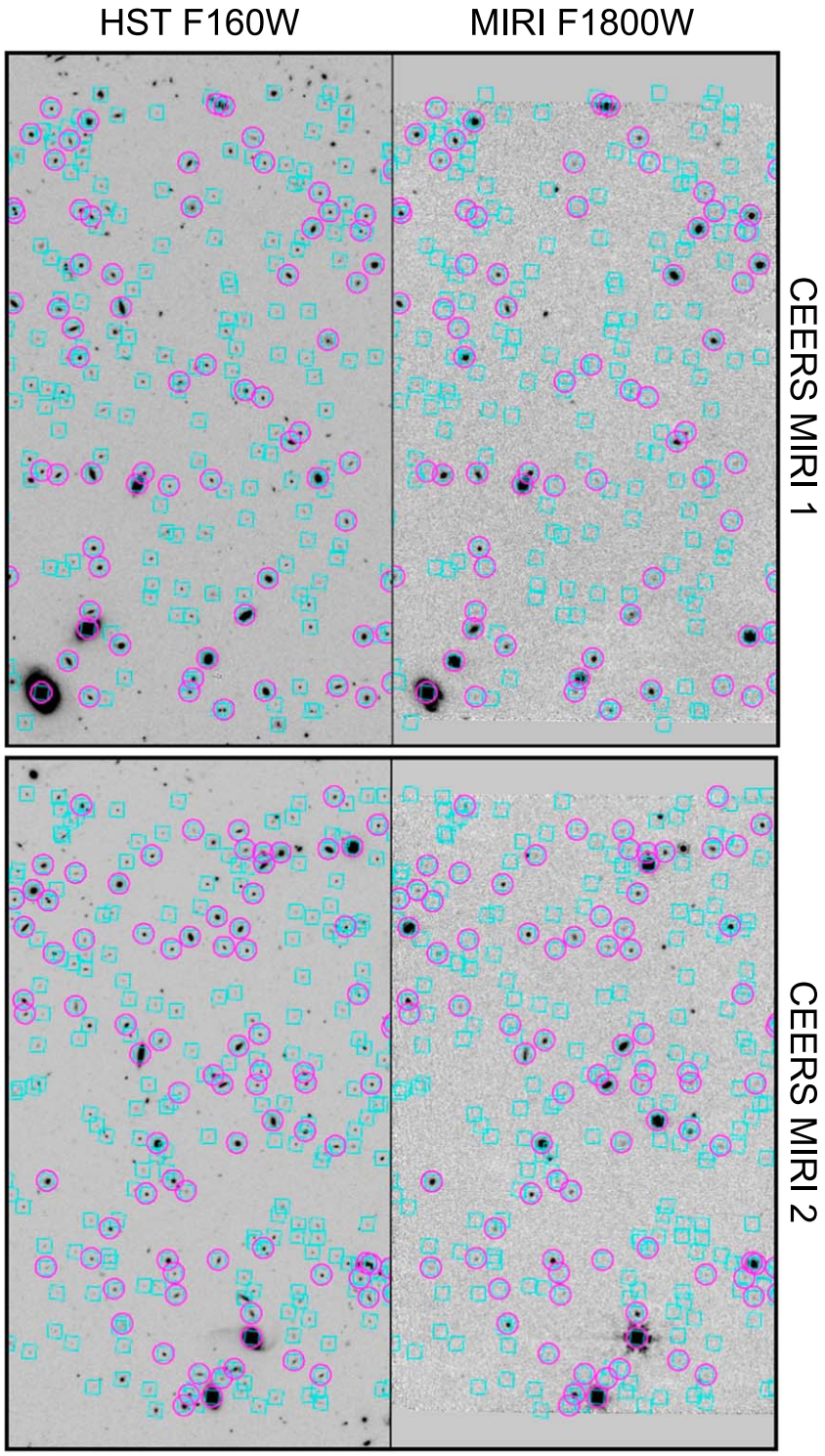

Figure 1. HST F160W (left) and MIRI F1800W (right) for fields CEERS MIRI 1 (top row) and CEERS MIRI 2 (bottom row). Blue squares are sources with m(F160W) < 26.6 mag at z < 2, and purple circles (diameter of $2\farcs6$ for scale) are sources with S/N (rest-frame 7.7 μm) > 4.

The distinction in notation primarily serves as a reminder of our methodology for measuring the 7.7 μm flux in this study. To calculate $\langle F_{770} \rangle$ we use

$$\langle F_{770} \rangle = \frac{\int_{c/8.8\mu\mathrm{m}}^{c/6.4\mu\mathrm{m}} (T(\nu)F_\nu)/\nu \;\; d\nu}{\int_{c/8.8\mu\mathrm{m}}^{c/6.4\mu\mathrm{m}} T(\nu)/\nu \;\; d\nu}. \quad (1)$$

Here, F_ν and ν are the flux and frequency from the model SEDs output from Case 1 shifted to the rest frame. $T(\nu)$ is the MIRI F770W transmission filter taken from the Spanish Virtual Observatory (Rodrigo et al. 2012; Rodrigo & Solano 2020). We then measure the PAH luminosity as

$$L_{770} = 4\pi (D_L)^2 \langle F_{770} \rangle \nu_{\langle 7.7\mu\mathrm{m} \rangle}. \quad (2)$$

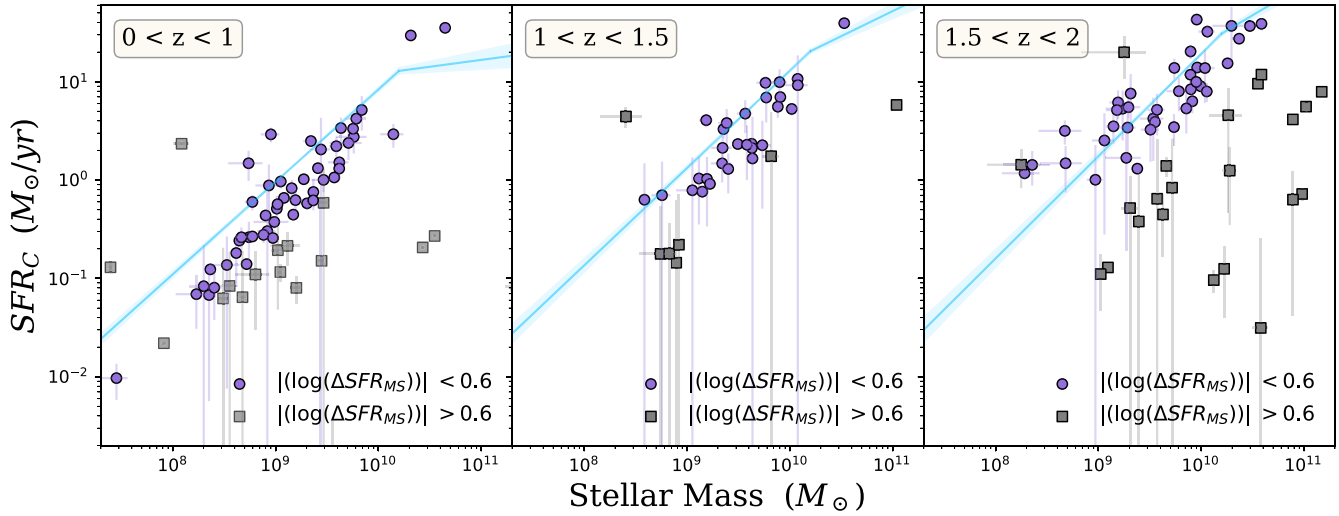

Figure 2. SFR–mass relation for the galaxies in our samples compared to the star-forming main sequence. The panels show the SED-measured SFRs from CIGALE (SFR_C; Section 4.1) as a function of the estimated stellar masses in different redshift bins (as labeled). The blue line indicates the star-forming main sequence and the uncertainty in the relation in the blue shaded region from Whitaker et al. (2014).

Table 1
Summary of Sample Selection

Selection Criteria	No. of Galaxies
Initial sample with m(F160W) < 26.6 mag	816
Redshift range: $0 < z < 2$	607
MIRI brightness: S/N (rest-frame 7.7 μm) > 4	189
Sufficient coverage: MIRI `mosaicFlag` = 0	173
Not an AGN: AGN flag = 0	173
Final sample with $\lvert(\log(\Delta SFR_{MS}))\rvert < 0.6$	120

Here, D_L is the luminosity distance, calculated with the *astropy.cosmology* package in PYTHON, and $\nu_{7.7}$ is the rest-frame frequency at 7.7 μm ($\nu_{7.7} = c/7.7\ \mu$m).

We note that the rest-frame 7.7 μm contains the bright emission from the 7.7 PAH complex *and* the dust continuum (and we make no correction for the latter). L_{770} primarily does not have any contribution from the stellar continuum for star-forming galaxies such as those in our sample. However, there are a few exceptions that we discuss in Section 6.3. The dust continuum is estimated to contribute up to 10% of the emission compared to the 7.7 μm PAH luminosity for MIRI F770W (Chastenet et al. 2023; Whitcomb et al. 2023). This value is an approximation for star-forming galaxies at low redshift from the SINGS sample, which will require further study with JWST/MIRI to determine if this holds for fainter galaxies at higher redshifts. With this, we will assume that $\langle F_{770} \rangle$ is dominated by the equivalent width of the 7.7 μm PAH emission in star-forming galaxies at $z < 2$. We explore the impact of the dust continuum on our results in Section 6.3 and Appendix B.

We estimate the observed FUV luminosity following the same definition as in Kennicutt & Evans (2012) with a central wavelength of 0.155 μm and $\Delta\lambda = 0.2\ \mu m$. We integrate the fitted models from CIGALE using

$$F_{\mathrm{FUV_{obs}}} = \int_{0.135\mu\mathrm{m}}^{0.175\mu\mathrm{m}} F_\nu\, d\nu. \quad (3)$$

The observed FUV luminosity is then corrected for dust using the Case 2 model output FUV attenuation (A(FUV)). This yields

$$F_{\mathrm{FUV}} = F_{\mathrm{FUV_{obs}}} \times 10^{0.4 \times A(\mathrm{FUV})}. \quad (4)$$

Here, the dust-corrected FUV luminosity is $L_{\mathrm{FUV}} = 4\pi (D_L)^2 F_{\mathrm{FUV}}$.

4.3. Estimate of Uncertainties on Derived Quantities

We estimate the uncertainties on derived quantities, including the rest-frame observed FUV and 7.7 μm luminosities using a Monte Carlo (MC) simulation. To do this, we perturb the photometry for each galaxy in the catalogs 1000 times with a random value (R) taken from a normal distribution with mean $\mu = 0$ and variance $\sigma^2 = 1$, i.e., $N(\mu = 0,\ \sigma^2 = 1)$, then multiplied by the observed errors, f_{err}, and added to the measured flux density, f. This yields the following equation

$$f_{\mathrm{new}} = f + f_{\mathrm{err}} \times R. \quad (5)$$

In each iteration, we refit the perturbed galaxy SED using the same method outlined in Section 4.1. Following the same equations in Section 4.2, we then measure L_{770} and the observed FUV luminosity from each newly modeled SED for each source. After the 1000 iterations are complete, we measure the 1σ standard deviation, which is used as our uncertainty estimate on these quantities. For uncertainty in the dust-corrected FUV luminosity (L_{FUV}), we also consider the model estimated uncertainties in A(FUV) and propagate accordingly for each source.

5. Results

In this Section we examine the correlation between the rest-frame dust-corrected FUV luminosity and the rest-frame 7.7 μm luminosity. Our goals for this section are to assess the application of the 7.7 μm luminosity as a tracer of star formation for the following cases: (1) retrieving information on the total SFR when only MIRI data are available, and (2) the PAH luminosity as a tracer of obscured star formation when FUV data are also available. From the analysis we measure a

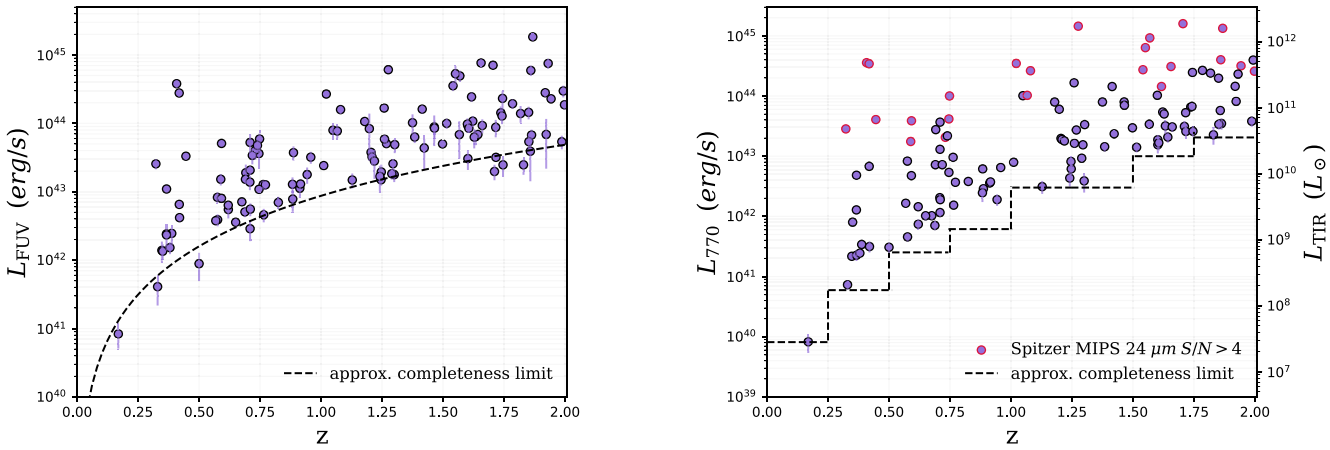

Figure 3. Left: dust-corrected UV luminosity $L_{\rm FUV}$ compared to redshift for our final sample. The black dashed line shows the approximate 90% completeness limit of the UVCANDELS data. Right: L_{770} vs. redshift for our final sample. The right ordinate shows the corresponding $L_{\rm TIR}$ estimated from our SED modeling. The black dashed line in each redshift bin indicates the 4σ limit with MIRI.

Table 2
CIGALE Parameters Used for SED Fitting

Module	Parameter	Input Value(s)
Star formation history: SFR(t) $\propto \frac{t}{\tau^2} \times \exp\left(\frac{t}{-\tau}\right)$	τ [Myr]	0.1, 0.5, 1.0, 5.0
	t [Myr]	0.5, 1.0, 3.0, 5.0, 7.0
Simple stellar population: Bruzual & Charlot (2003)	IMF	Chabrier (2003)
	Metallicity	$Z_\odot = 0.02$
Dust attenuation: Calzetti et al. (2000)	$E(B-V)_l$	0.1, 0.3, 0.5, 0.8
	UV bump amplitude	0.0, 1.5, 3.0
	power-law slope	−0.3, −0.1, 0.0
Dust emission: Draine et al. (2014)	$q_{\rm pah}$	0.47, 1.77, 3.19, 4.58, 5.95, 7.32
	$u_{\rm min}$	0.2, 1.0, 5, 10, 20, 35
	γ	0, 0.005, 0.1, 0.02
Redshift	z	Fixed at z of Stefanon et al. (2017) and N. Hathi (2024, private communication)

Note. The default CIGALE values were used for parameters not listed in this table.

"single-wavelength" calibration between the 7.7 μm luminosity and the dust-corrected FUV luminosity (Section 5.2). We then also derive a "multiwavelength" relation between the dust-corrected FUV luminosity and a linear combination of the observed (uncorrected for dust) FUV and 7.7 μm luminosities (Section 5.3). In both cases, we evaluate the performance of our calibrations by comparing the estimated SFRs derived from both single and multiwavelength SFR calibrations with SED model estimated SFRs from our work and the independent analysis from the Stefanon et al. (2017) catalog.

5.1. The PAH–FUV Relation

We compare the rest-frame dust-corrected FUV luminosity with the rest-frame 7.7 μm luminosity in Figure 5. In this figure we introduce an additional top abscissa that shows the SFR corresponding to the dust-corrected FUV using the relation from Kennicutt & Evans (2012) assuming a constant SFR over the past 100 Myr, which is corrected for a Chabrier (2003) IMF using the conversion factor from Madau & Dickinson (2014).

To characterize the correlation between the dust-corrected FUV and PAH luminosities, we fit a linear relation (where the slope is a free parameter) and unity relation (where the slope is set to one). Specifically, we define the linear relation such that $\log L_{770} \propto k \times \log L_{\rm FUV}$, where k is a constant of proportionality. The unity relation then has $k = 1$. The linear fits presented in this work are measured using LINMIX, a PYTHON package that uses a hierarchical Bayesian approach from Kelly (2007) and accounts for uncertainties on both the dependent and independent variables (see also Feigelson & Babu 1992). LINMIX accounts for heteroscedastic data, correlated measurement errors, and intrinsic scatter (see Kelly 2007). From these we obtain

$$\log(L_{770}) = (1.27 \pm 0.04)\log(L_{\rm FUV}) - (12.1 \pm 2), \quad (6)$$

where the luminosities have units of erg s^{-1}. The unity fits are measured using *curve_fit* from SCIPY (Virtanen et al. 2020), which gives

$$\log(L_{770}) = \log(L_{\rm FUV}) - (0.286 \pm 0.001). \quad (7)$$

The fitted unity and linear relations are shown as the green and purple lines, respectively, in Figure 5. The deviation from unity at the luminosity limits of our sample suggests that for these regimes the PAH emission has a complex relation with the SFR. We further explore this in Section 6.1.

We test the unity and linear relations above using the Akaike information criterion (AIC). The AIC considers an improvement in the likelihood of the fit of a model with additional parameters, where a model is adopted if the change in the log-likelihood increases by more than the change in twice the number of parameters. We find that the linear fit shows an improved log-likelihood by a factor of ∼1.4 when we have added only one additional parameter. This indicates that the data favor the linear model over the unity model. For this reason we measure the scatter about the linear relation as opposed to the unity in the bottom panel of Figure 5. Formally, we measure a scatter of 0.29 dex.

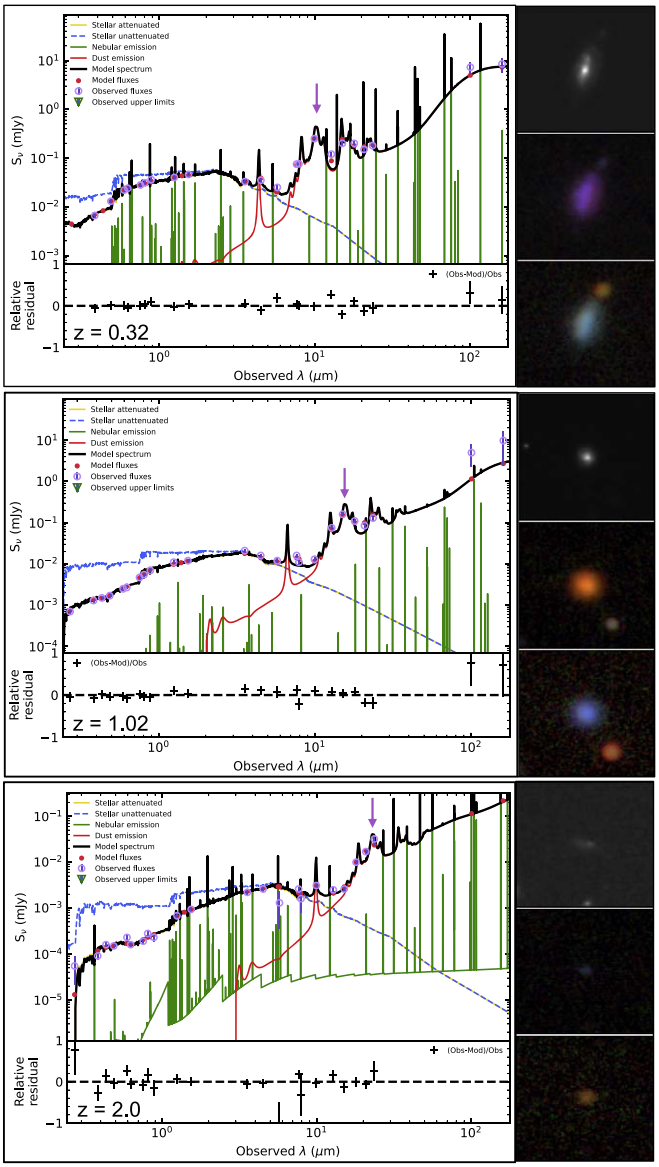

Figure 4. Each panel shows an example of the best-fit SEDs from our Case 2 fits with CIGALE for sources in the selected sample in order of increasing redshift (top to bottom). The data in each plot show the flux densities and their uncertainties from the catalogs in Section 2 with each curve representing different model components (see panel legend). The location of the observed 7.7 μm feature is highlighted in each panel by the purple arrow. To the right of each panel are $10'' \times 10''$ postage stamps of the CEERS HST F160W (top), composite RGB image of JWST/MIRI F1000W (B) + F1280W (G) + F1500W (R); (middle), and composite RGB image of JWST/MIRI F1500W (B) + F1800W (G) + F2100W (R); (bottom). The MIRI images shift in color as the 7.7 μm PAH feature redshifts through the different MIRI bands. At $z = 0.32$, the 7.7 μm PAH feature falls in the F1000W band, with an additional PAH feature that peaks at F1500W, which makes the image "purple." At $z = 1.02$, the 7.7 μm PAH feature falls in the F1500W band, making the middle image "red" and the bottom image "blue". At $z = 2.0$, the PAH feature falls in the F2100W band, making the bottom image "red."

5.2. Single-wavelength SFR Calibration

Motivated by the strong correlation between the rest-frame mid-IR luminosity and the rest-frame dust-corrected FUV luminosity, we derive a "single-wavelength" calibration of SFR from the 7.7 μm luminosity. We convert L_{770} to $L_{\rm FUV}$ using the linear fit from Equation (6), which was selected by the AIC as mentioned in Section 5.1. We then derive SFR from $L_{\rm FUV}$

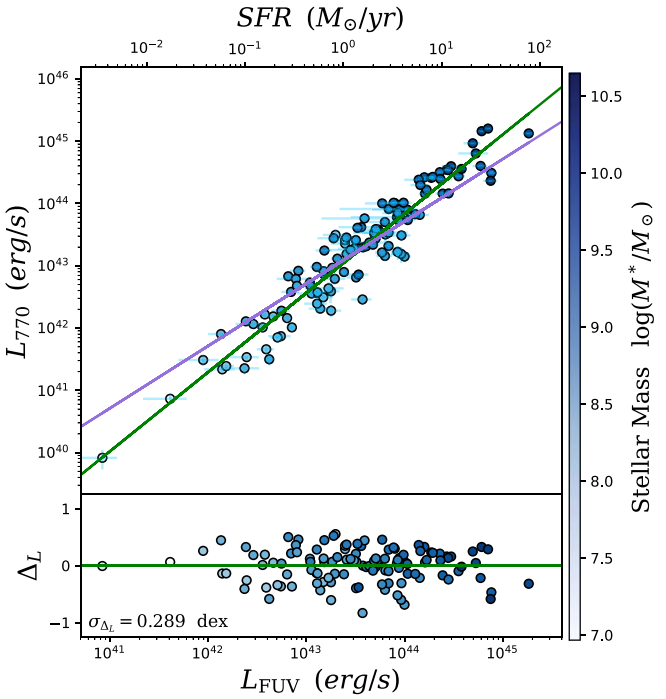

Figure 5. Top: L_{770} compared to the dust-corrected FUV luminosity. The top axis shows the corresponding SFR derived following Kennicutt & Evans (2012) corrected for a Chabrier (2003) IMF. The green line is the linear relationship (as described in Equation (6)), and the purple line shows the the unity relation (as described in Equation (7)). Bottom: scatter about the linear fit where $\Delta L = \log(L_{770}) - \log(L_{\rm Linear})$, with $\sigma = 0.289$ dex. The data are colored by stellar mass in log scale.

following the relation from Kennicutt & Evans (2012) corrected for a Chabrier (2003) IMF. The resulting conversion is

$$\log({\rm SFR}_{7.7\ \mu{\rm m}}) = (0.787 \pm 0.03)\log(L_{770}) - (33.8 \pm 2), \quad (8)$$

where the SFR is measured in $M_\odot\ {\rm yr}^{-1}$ and the luminosity is again in units of erg s^{-1}.

To test the performance of this calibration we compare the estimated values for ${\rm SFR}_{7.7\ \mu{\rm m}}$ from Equation (8) to ${\rm SFR}_{\rm C}$ and independently measured SFR estimates from the Stefanon et al. (2017) catalog estimated with method 2a from Mobasher et al. (2015; ${\rm SFR}_{\rm M15}$) in Figure 6. The work from Mobasher et al. (2015) estimated ${\rm SFR}_{\rm M15}$ by modeling the multiwavelength photometry from the Stefanon et al. (2017) catalog using a variety of methods. We adopt method "2a" from Mobasher et al., which was fixed to a Chabrier (2003) IMF and left star formation history (SFH), metallicity, extinction, and population synthesis code as free parameters. We selected this SFR estimate from the Stefanon et al. (2017) catalog since it was the most similar to our work. We measure the scatter between the model estimated SFRs to the estimates from our calibration to find $\sigma_{\Delta{\rm SFR}} = 0.24$ dex for ${\rm SFR}_{\rm C}$ and 0.36 dex for ${\rm SFR}_{\rm M15}$, respectively. We note that there appears to be an offset in the plot where the ${\rm SFR}_{\rm C}$ values are higher than ${\rm SFR}_{7.7\ \mu{\rm m}}$ at lower SFRs, but we expect this to be a result of the star formation histories used by the SED modeling (see Appendix A). Regardless, the measured scatter about the linear relation in Figure 6 is tight across all 7.7 μm luminosities.

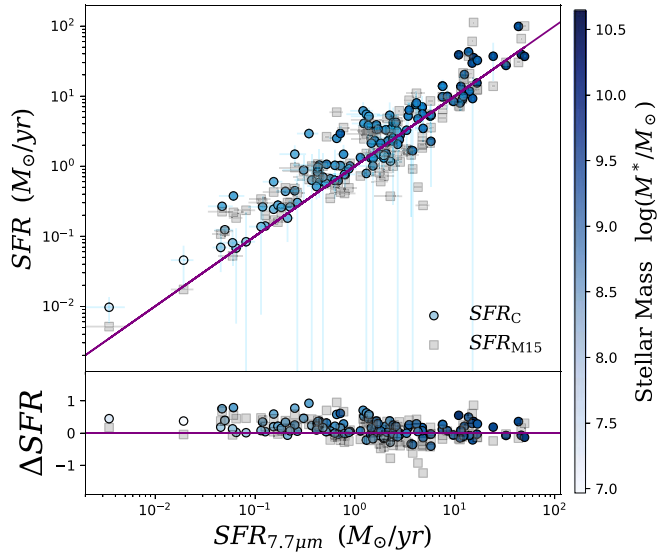

Figure 6. Top: SFR derived from the single-wavelength calibration compared to SFR_C (the circular points colored by stellar mass estimated by CIGALE) and SFR_{M15} (represented with the gray squares). The dark purple line shows the one-to-one relation. Bottom: measured scatter about the one-to-one relation, which is measured by $\Delta SFR = \log(SFR_{7.7\,\mu m}) - \log(SFR)$. The measured $\sigma_{\Delta SFR}$ for SFR_C and SFR_{M15} is 0.24 dex and 0.36 dex, respectively.

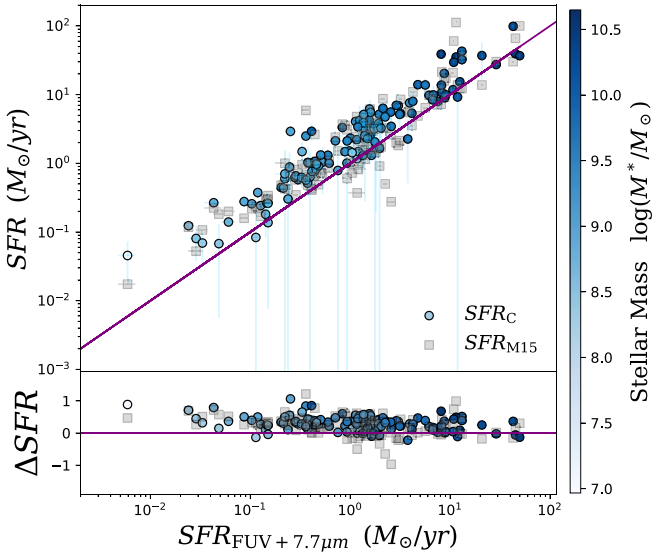

Figure 7. Top: SFR derived from the multiwavelength calibration (shown in Equation (10)) compared to SFR_C (represented with the circular points colored by stellar mass from CIGALE), and SFR_{M15} (represented with the gray squares). The dark purple line shows the one-to-one relation. Bottom: measured scatter about the one-to-one relation, which is measured by $\Delta SFR = \log(SFR_{FUV}) - \log(SFR)$. The measured $\sigma_{\Delta SFR}$ for SFR_C and SFR_{M15} is 0.21 dex and 0.27 dex, respectively.

5.3. Multiwavelength SFR Calibration

We next consider a case where the total SFR is a combination of the unobscured SFR measured from the observed rest-frame FUV and obscured SFR measured from the 7.7 μm luminosity. In principle, there should exist some energy balance between these two variables as they trace the total emission from the young massive stars (e.g., Calzetti et al. 2007; Kennicutt et al. 2007). Motivated by this concept, we model the total intrinsic FUV luminosity as a multiwavelength, linear combination of the observed FUV luminosity (uncorrected for dust attenuation) and the 7.7 μm luminosity using

$$L_{\rm FUV} = L_{\rm FUV,obs} + \eta L_{770}. \quad (9)$$

Equation (9) is similar to the linear combination of $L_{\rm TIR}$ and the FUV luminosity in Equation (11) from Kennicutt & Evans (2012) and is in the simplest form. In principle, there could be additional factors that manifest as higher-order polynomials, which we ignore here. Using *curve_fit* from SCIPY we find that $\eta = 0.732 \pm 0.002$.

Using this result, we establish a "multiwavelength" calibration for the SFR based on the linear combination of the observed FUV and the mid-IR luminosity using the FUV–SFR relation from Kennicutt & Evans (2012) corrected for a Chabrier (2003) IMF. This yields

$$\log {\rm SFR}_{\rm FUV+7.7\mu m} = \log(L_{\rm FUV_{obs}} + \eta L_{770}) - 43.32, \quad (10)$$

where $\eta = 0.732 \pm 0.002$ from above, the SFR is in units of $M_\odot\,{\rm yr}^{-1}$, and the luminosities are in units of erg s^{-1}.

We compare the estimated SFRs from the multiwavelength calibration to the model estimated SFRs (SFR_C and SFR_{M15}) in Figure 7. We measure the scatter between the model estimated SFRs to that of the multiwavelength calibration, which results in $\sigma_{\Delta SFR} = 0.21$ dex for SFR_C and 0.27 dex for SFR_{M15}. We again observe an offset between the model estimated SFRs and the estimates from the multiwavelength calibration at SFRs below roughly $10^{-1}\,M_\odot\,{\rm yr}^{-1}$, which is attributable to the SFH used on the models in addition to varying galaxy properties. We explore the effects of SFH on SFR_C (see Appendix A), and the galaxy properties that can contribute to the observed offset at these SFRs in Section 6.1.2.

6. Discussion

MIRI provides a new opportunity to quantify dust-obscured star formation for high-redshift galaxies that are much fainter than those previously accessible by any of the JWST predecessors. As we have demonstrated above, the rest-frame mid-IR luminosity measured from broadband JWST/MIRI data (L_{770}) correlates strongly with the most recent star formation activity traced by the FUV luminosity. We discuss the physical process behind the FUV–PAH correlation in Section 6.1. We then discuss what types of galaxies depart from the FUV–PAH correlation in Sections 6.1.2 and 6.1.3. We place our results in the context of previous calibrations of the PAH luminosity in Section 6.2. Finally, we discuss some caveats that can impact the interpretation of our results in Section 6.3.

6.1. The Relation between the PAH Emission and SFR

In this section we consider the relation between the 7.7 μm luminosity and the SFRs in three different regimes: galaxies with "moderate" SFRs ($\sim$10–30 $M_\odot\,{\rm yr}^{-1}$), where the galaxies have PAH luminosities that are nearly proportional to the total SFR; "low" SFRs ($\lesssim 10\,M_\odot\,{\rm yr}^{-1}$), where the PAH luminosities of the galaxies are low compared to the total SFRs; and "high" SFRs ($\gtrsim 30\,M_\odot\,{\rm yr}^{-1}$), where the PAH luminosities again depart from the unity relation with FUV-based SFRs as shown in Figure 5. Each SFR regime is likely a result of different physical effects in galaxies that impact this relation.

6.1.1. Relation at Moderate SFRs

Figure 5 highlights the capability of the PAH emission to trace the total SFR, where we compare the rest-frame 7.7 μm emission to the SFR from the dust-corrected FUV luminosity.

We find that more than half of our sample (60%) has SFRs of between 10 and 30 $M_{\odot}\,\mathrm{yr}^{-1}$, which is where the linear and unity correlations between the dust-corrected FUV luminosity and the PAH luminosity intersect. Such galaxies provide important case studies in which the 7.7 μm PAH luminosity is a direct tracer the total star formation rate. This is consistent with previous studies that focused on the relation between PAH luminosity and the SFR (e.g., Houck et al. 2007; Shipley et al. 2016; see Section 6.2 below). Here, the implication is that the 7.7 μm luminosity is directly proportional to the SFR. The scatter in the relations is also small, with $\sigma_{\Delta\mathrm{SFR}} \simeq 0.3$ dex, which is likely a systematic floor to the (combined) accuracy of the UV and mid-IR SFRs.

To further investigate the reasoning behind this occurrence in our sample for this regime, we must first examine the properties of these sources. For this subset of our sample with SFR $\approx$ 10–30 $M_{\odot}\,\mathrm{yr}^{-1}$, the galaxies are optically thick in the visual (the average dust attenuation is $A_V \simeq 1.9$) with an average stellar mass of 9.5 $\log(M^*/M_{\odot})$. This is typical of galaxies at these masses/SFRs, where most of the star formation in such galaxies is obscured. For example, Whitaker et al. (2017) find that ~70%–90% of star formation is obscured for galaxies in this redshift and mass range. This is significant in the era of JWST as more obscured galaxies are being discovered due to the unprecedented sensitivity. It is also prudent to consider the galaxy properties in which such an assumption would not be valid, which we explore below.

6.1.2. Relation at Low SFRs

From Figure 5 we observe that at low PAH luminosities ($L_{770}/(\mathrm{erg\,s}^{-1}) > 10^{42}$) the slope of the relation between the SFR and L_{770} is steeper than the unity relation. This means that the 7.7 μm PAH luminosity is weaker (at fixed SFR or at fixed mass), and is less of a direct tracer of the total SFR. This occurs at stellar masses of approximately $M < 10^8 M_{\odot}$.

Observations of local galaxies show that the PAH emission is significantly weaker and less correlated with star formation for metal-poor galaxies. In such objects the PAH emission drops by up to a factor of 30 for metal-poor H II regions compared to metal-rich counterparts (Engelbracht et al. 2005; Calzetti et al. 2007). Due to the lack of necessary data to determine the metallicity content of our sample, we approximate the metallicity using a mass–metallicity relation (MZR) from Zahid et al. (2011). We find that these low-mass sources have metallicities of 0.4 dex below solar, and therefore we expect that the lower 7.7 μm luminosities for low-mass galaxies is a result of lower metallicities. This is consistent with previous work for nearby galaxies, as seen in Figure 3 of Calzetti et al. (2007) for H II regions in galaxies with intermediate and low metallicities ($12 + \log(\mathrm{O/H}) < 8.35$, i.e., less than about 0.5 dex of the solar value). We note that the scatter in both of the SFR calibrations derived in this work are remarkably constant (it remains close to ≃0.3 dex) even at low stellar masses. This likely implies there is a common cause to the decrease in the 7.7 μm luminosity—such as the galaxies having lower metallicity—rather than some other mechanism that would lead to larger scatter.

We consider other physical phenomena in galaxies besides low metallicity that could cause the PAH emission to not be capable of tracing the total SFR in these low-mass galaxies. One alternative is that the lower PAH emission is caused by hard ionizing radiation fields that destroy the molecules, or delayed formation of PAH molecules in AGB stars (Chastenet et al. 2023). Both of these require timescale arguments; we expect the galaxies to have a wider range of ages than allowed by the relatively low scatter between L_{770} and SFR in our sample. Another possible explanation as to why the PAH luminosity does not directly trace the total SFR for lower-mass/SFR galaxies is that the degree of obscuration is lower in these galaxies. For 3 of the 14 low-mass sources, we observe that these galaxies experience low attenuation, with ($A_V \simeq 0.3$). As such, the dust and PAH molecules do not trace the majority of the light emitted by star-forming regions in galaxies (Hirashita et al. 2001). However, the majority of the low-mass sources (11/14) are more obscured ($A_V > 1$). This evidence suggests that lower metallicity is the more probable cause as to why the measured PAH luminosity is less correlated with the total SFR.

6.1.3. Relation at High SFRs

Figure 5 shows that at high PAH luminosities ($L_{770}/(\mathrm{erg\,s}^{-1}) > 10^{44}$) the slope of the relation to the SFR is shallower than the unity relation, which indicates that the 7.7 μm PAH luminosity is departing as a direct tracer of the total SFR. Given the SFR, this occurs for galaxies with stellar masses of above approximately $10^{10.5} M_{\odot}$. However, we note again that the scatter in the relation between L_{770} and the SFR remains relatively small, $\sigma_{\Delta\mathrm{SFR}} \simeq 0.3$ dex, which implies that the cause of this shallower relation between L_{770} and the SFR is not a result of increased scatter.

In these higher luminosity regimes, there are two primary reasons why the strength of the PAH features could be expected to diverge as a tracer of the total SFR. One reason would be that the strength of PAH emission is suppressed in ultraluminous IR galaxies (ULIRGs) with $L_{\mathrm{TIR}} > 10^{12} L_{\odot}$, as has been seen in some studies (Pope et al. 2008; Takagi et al. 2010; Rieke et al. 2015). A second reason is that these galaxies have built up a population of older, more-evolved stellar populations that are contributing to the heating of the PAH molecules (Zhang & Ho 2023), where it can be possible for both effects to contribute. We favor the second scenario as more applicable to our sample based on our discussion in Appendix C (see also Figure 11), where we explore trends between the ratio of the dust-corrected FUV luminosity to the L_{770} luminosity as a function of stellar mass and A(FUV). We observe the L_{770} luminosity is higher than the dust-corrected FUV for galaxies at larger stellar mass, which indicates that there is an increase in the fraction of the PAH luminosity that is not correlated with the short-lived stellar populations that drive the UV emission. If instead there were an increase in the suppression of PAH molecules in ULIRG-type galaxies in our sample, we would anticipate the opposite outcome for higher stellar masses. Again, both processes may be at play, but the lower scatter between L_{770} and the SFR even for high-SFR galaxies indicates most galaxies follow the same trends. One caveat here is that we excluded galaxies in the "starburst" phases that lie more than 0.6 dex above the star-forming main sequence, but could not identify starbursts that might lie within the star-forming main sequence. These galaxies could contribute to the observed trends or may show differing trends between L_{770} and the total SFR, which we will explore in future work.

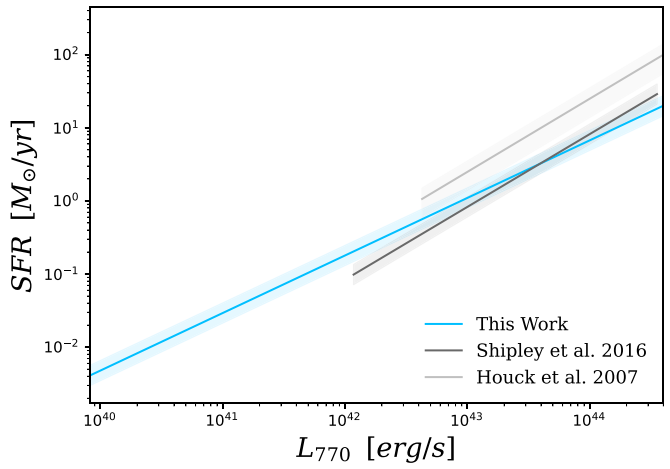

Figure 8. Comparison of the L_{770} and SFRs from our work and previous works in the literature. There is good agreement where the calibrations overlap, in particular with the relation from Shipley et al. (2016), who used Spitzer/IRS data to predict the relation between the MIRI F770W rest-frame luminosity and SFR. All SFR estimates from the literature are corrected to a Chabrier (2003) IMF. The shaded regions around each line are the 1σ dispersion reported on each relation.

6.1.4. Evolution with Redshift

We tested for any evolution in redshift in the relation between L_{770} and SFR. We note that we have a limited dynamic range in both L_{770} and redshift (see Figure 3), but it is useful to determine if the relation evolves with time and how. We split our sample into two redshift bins from where our sample is complete (10^{43} erg s^{-1}): $0.32 \leqslant z \leqslant 1.1$ and $1.1 \leqslant z \leqslant 2$. We then refit Equation (6) for each bin and measure slopes of 1.01 ± 0.13 and 1.11 ± 0.12, respectively (1.11 ± 0.07 for the sample above the completeness limit). We determine that there is no evidence for evolution in the relationship between L_{770} and SFR for our sample.

6.2. Comparison to Literature

We compare our derived single-wavelength calibration to previous calibrations from literature in Figure 8. To ensure an accurate comparison between calibrations, we corrected all calibrations to a Chabrier (2003) IMF. There are other calibrations from literature (Hernán-Caballero et al. 2009; Xie & Ho 2019) that are not considered for our comparison due to the differences in sample selection, where these other studies include AGN and/or very high-luminosity objects (e.g., bright ULIRGS) with a much larger SFR range that is not included in our sample.

Shipley et al. (2016) derived a relation between the PAH luminosities and the Hα emission line, and used the relation between Hα and SFR following Kennicutt & Evans (2012). Shipley et al. used Spitzer/IRS spectroscopy of relatively low-redshift galaxies, with $z < 0.4$, where our sample probes much smaller SFRs at these same redshifts. To compare the calibration to our results, we select Equation (18) from Shipley et al. (2016) and correct it to a Chabrier (2003) IMF. The linear single-wavelength calibration was derived with a synthesized JWST/MIRI F770W filter, which was determined to be most similar to this work. We find that our calibration is consistent with the results from Shipley et al. within the 68% uncertainties in the range where they are calibrated (see Figure 8). Shipley et al. (2016) concluded that the 7.7 μm PAH feature directly traces the total SFR measured from dust-corrected Hα, with a unity relation. Here, we find that the relation between 7.7 μm is linear, with a slope of 0.78 (subunity). The main reason for this difference is that we are considering galaxies over a larger range in luminosity, where we consider different effects that can impact the PAH emission (see Section 6.1). In addition, Shipley et al. (2016) used Hα-derived SFRs, which can probe the SFR on shorter timescales than the FUV. If we refit our linear relation derived in Equation (6) to a subset of our sample at PAH luminosities that are comparable to Shipley et al. ($L_{770} \geqslant 1 \times 10^{43}$ erg s^{-1}), we would measure a slope of 1.11 ± 0.07. This is consistent with the single-wavelength calibration derived from Shipley et al., indicating that our ability to probe fainter SFRs with JWST/MIRI reveals the subunity relation at these lower luminosities.

Houck et al. (2007) derived a relationship between the PAH luminosity and the total-IR luminosity, and then used the $L_{\rm TIR}$–SFR relation from Kennicutt (1998) to derive a single-wavelength SFR calibration for the PAH luminosity. The sample for their work spanned redshifts ($z < 0.5$) and included galaxies with a range of $L_{\rm TIR}$ and type, such as AGN, ULIRGs, and starburst galaxies. To compare the results from Houck et al. to our calibration, we adjust the Kennicutt (1998) $L_{\rm TIR}$–SFR relation to the one from Kennicutt & Evans (2012; accounting for the updated calibration and the Chabrier 2003 IMF). In general, the Houck et al. results return larger SFR values than the ones from both Shipley et al. (2016) and this work. This is evident in Figure 8 as a small offset between the calibrations. The origin of this difference is likely related to the strength of the PAHs in different galaxies. For example, the PAH strength is observed to be weaker in AGN and ULIRGs (Takagi et al. 2010; Xie & Ho 2022).

Kirkpatrick et al. (2023) examined the relation between the PAH luminosity and $L_{\rm TIR}$ for a sample of galaxies in CEERS with MIRI. Kirkpatrick et al. measured the 6.2 μm luminosity ($L_{6.2}$) from the flux in the MIRI band closest in wavelength to rest-frame 6.2 μm. The results from this work found a roughly constant ratio of $L_{6.2}/L_{\rm TIR}$, albeit with a large scatter ($\sim$0.7 dex). This result is similar to what we observe in our sample with the 7.7 μm flux, but we acknowledge that further analysis of MIRI-detected galaxies with far-IR photometric data is needed.

6.3. Impact of Caveats and Assumptions

There are several important caveats that arise from our assumptions and modeling methods. Estimates of parameters with CIGALE (e.g., SFRs, stellar mass, and dust attenuation) can be less accurate for galaxies with high dust obscuration (Pacifici et al. 2023). This is one reason that we follow the recommendations of Pacifici et al. (2023) and use the measured properties from SED models that include FUV to far-IR photometry. Given that less than 1% of our sources have any Hershel/PACS 100 or 160 μm detections, the FUV attenuation is predominately constrained by the MIRI data. To test the effect of MIRI on FUV attenuation estimates from CIGALE, we reran the models from SED modeling Case 2 (as described in Section 4.1) removing the MIRI data from the fits. We then compared the FUV attenuation estimates and found that the uncertainty in the FUV attenuation increases by an order of magnitude when the MIRI data are excluded. Both of our calibrations are dependent on dust-corrected FUV luminosity, which was corrected for dust with A(FUV) output from

CIGALE. This is why the MIRI data are included in our Case 2 SED modeling. We plan to study this further in a future work where we will explore the mid-IR luminosity and SFR relation with SFR tracers that are less sensitive to attenuation compared to the FUV.

We also consider if there is any stellar continuum contribution to L_{770}, which would cause our estimate to not strictly trace the 7.7 μm PAH luminosity for our selected sample. To test this, we used the CIGALE-model SED outputs that include the individual contributions from continuum, nebular, and dust spectra to the total SED (example shown in the top panel of Figure 4). For sources with mid-IR luminosities above $L_{770} \gtrsim 1 \times 10^{43}$ erg s^{-1}, the difference between the "dust" SED (i.e., the emission that includes emission from the PAH features and thermal dust emission) and the total SED is approximately 0.009 dex (i.e., $\simeq$2%). Therefore, we conclude that the galaxies in our sample that are above these luminosities have a negligible contribution from the stellar continuum. For sources below $L_{770} \lesssim 1 \times 10^{43}$ erg s^{-1}, the PAH strength is weaker, and the stellar continuum can account for more of the light. To quantify this, we examined the 14 sources below this luminosity limit and found that 5 appear to have small, but non-negligible contribution of the stellar continuum to the L_{770} through visual inspection of the best-fit SEDs. We recalculate L_{770} using Equation (1) with the dust SED only (e.g., the red-colored curves in Figure 4) from our Case 1 best-fit SED models. This reduces the L_{770} values by an average of 0.06 dex (i.e., 15%) for these five galaxies. The PAH luminosity even in these cases accounts for the majority ($\geqslant$85%) of the total mid-IR light. Considering the full sample, this affects the derived calibration by only 0.02 dex (i.e., 5%).

We have assumed that the 7.7 μm PAH luminosity can be reasonably measured by the average flux density in the rest-frame MIRI F770W bandpass. Whereas, other studies have quantified the PAH luminosity as the integral of the emission in the lines directly. We test the validity of our assumption in Appendix B, but will briefly describe it here. We used the estimated values of the 7.7 μm luminosity from Kirkpatrick et al. (2023; $L_{7.7}$), which excludes the continuum emission and integrates over the emission of the line; this is described in Section 4.2 of their work. We then compared L_{770} to $L_{7.7}$ in Figure 10. We find there is a constant offset between the lines of 0.67 dex and a tight scatter of 0.24 dex. This offset is expected given the difference in the methods. In this work we compute $\nu\langle f_\nu \rangle$, in contrast to Kirkpatrick et al. (2014) who calculated the line flux as $F = \int F_\lambda \, d\lambda$. In Appendix B we illustrate that this will lead to an offset of approximately 0.6 dex, which accounts for the near-constant offset (measured to be 0.67 dex) with a tight scatter.

Lastly, our selection of the MIRI F770W bandpass is arbitrary, as we could have used any bandpass that captures the 7.7 μm PAH emission with Equation (1). To test this, we use other MIRI bandpasses and redshift the Case 1 SEDs such that the observed wavelength of the 7.7 μm feature lies in the center of a MIRI bandpass (for F1000W, F1500W, F1800W, and F21000W). We then measure the average flux following a similar methodology for F770W with Equation (1). We compare the average fluxes calculated with these MIRI bandpasses to that from $\langle F_{770} \rangle$. We find zero offset, and measure small scatters between the two of 0.008 dex, 0.006 dex, 0.011 dex, and 0.003 dex for F1000W, F1500W, F1800W, and F21000W, respectively. Therefore, the choice of the exact bandpass does not significantly effect our results.

7. Summary and Conclusions

In this paper, we studied the relation between the mid-IR luminosity at 7.7 μm and the SFR in star-forming galaxies at redshifts $0 < z < 2$. We used photometry from CEERS MIRI, UVCANDELS, and the Stefanon et al. (2017) multiwavelength catalog and fit the SEDs with CIGALE for a sample of 120 galaxies. With the SED fits we measure the rest-frame FUV luminosity (uncorrected for dust attenuation) and the rest-frame 7.7 μm luminosity from the average rest-frame flux in the MIRI F770W band (L_{770}). Using the best-fit estimates of the FUV attenuation (A(FUV)) from CIGALE, we correct the FUV luminosities for dust ($L_{\rm FUV}$). We then compare $L_{\rm FUV}$ and L_{770}, and from these we derive both a single-wavelength calibration between the SFR and L_{770} and a multiwavelength calibration between the SFR and a linear combination of the FUV luminosity (uncorrected for dust) and L_{770}. These calibrations are given in Equations (8) and (9). Our primary findings are as follows:

1. We find that the 7.7 μm PAH luminosity is well correlated with the dust-corrected FUV luminosity, following a linear relationship described by Equation (6).
2. Using the linear relationship between the 7.7 μm and dust-corrected FUV luminosities, we derive a single-wavelength SFR calibration that approximates the total SFR with the obscured SFR in Equation (8). We compare the SFR estimates from our single-wavelength calibration to model estimated SFRs from CIGALE and the SFRs from the independent catalog of Stefanon et al. (2017). The SFRs are well correlated with a scatter of $\sigma_{\Delta \rm SFR} = 0.24$ dex and 0.36 dex, respectively. We find that the total SFR can be approximated with the measured 7.7 μm luminosity reliably for galaxies over a wide range of luminosity and dust attenuation.
3. We derive a multiwavelength SFR calibration to estimate the (dust-corrected) FUV-based total SFR using a linear combination of the FUV luminosity (not corrected for dust) and the 7.7 μm luminosity. This method assumes an energy balance between the mid-IR and the FUV, which considers the total SFR as a combination of the unobscured and obscured SFR. We compare our SFR estimates from the multiwavelength calibration to model estimated SFRs from CIGALE and the Stefanon et al. (2017) catalog. From these we measure a scatter of $\sigma_{\Delta \rm SFR} = 0.21$ dex and 0.27 dex, respectively. The relatively small decrease in the scatter from the single-wavelength to the multiwavelength calibration implies that these are near the systematic accuracy of the total SFR using either calibration.
4. We compare L_{770} measured from the average flux in the rest-frame MIRI F770W bandpass to the independent estimate of the 7.7 μm luminosity ($L_{7.7}$) from Kirkpatrick et al. (2023) and measure a scatter of 0.24 dex. Our estimates are offset from $L_{7.7}$ by 0.67 dex, which is primarily due to difference in the methods (this agrees with our estimate that the offset should be 0.6 dex based on the width of the MIRI F770W filter and various assumptions). This is further evidence that the mid-IR emission at 7.7 μm is a good tracer of the SFR with a limiting systematic accuracy of approximately 0.2–0.3 dex.

This paper demonstrates the capability of the 7.7 μm PAH emission to trace star formation with JWST/MIRI. Future JWST surveys that explore the relation between the 7.7 μm

feature and star formation in variable environments (such as starburts, ULIRGs, or AGN) will provide more insight into obscured star formation and the behavior of the 7.7 μm PAH feature in galaxies across redshifts.

Acknowledgments

This work benefited from support from NASA/ESA/CSA James Webb Space Telescope through the Space Telescope Science Institute, which is operated by the Association of Universities for Research in Astronomy, Incorporated, under NASA contract NAS5-03127. Support for program No. JWST-ERS01345 was provided through a grant from the STScI under NASA contract NAS5-03127. This work is based on observations with the NASA/ESA Hubble Space Telescope obtained at the Space Telescope Science Institute, which is operated by the Association of Universities for Research in Astronomy, Incorporated, under NASA contract NAS5-26555. Support for program No. HST-GO-15647 was provided through a grant from the STScI under NASA contract NAS5-26555. This work benefited from support from the George P. and Cynthia Woods Mitchell Institute for Fundamental Physics and Astronomy at Texas A&M University. This research has made use of the Spanish Virtual Observatory project[27] funded by MCIN/AEI/10.13039/501100011033/ through grant PID2020-112949GB-I00. R.A.W. acknowledges support from NASA JWST Interdisciplinary Scientist grant Nos. NAG5-12460, NNX14AN10G, and 80NSSC18K0200 from NASA GSFC.

Software: astropy (Astropy Collaboration et al. 2013, 2018, 2022), CIGALE (Boquien et al. 2019), Source Extractor (Bertin & Arnouts 1996), Matplotlib (Hunter 2007), pandas (Reback et al. 2022), WEBBPSF (Perrin et al. 2012), JWST Calibration Pipeline (Bushouse et al. 2023), LINMIX (Kelly 2007).

Appendix A
Model Estimated Star Formation Rates

CIGALE calculates several different SFRs, including an instantaneous SFR and the SFR averaged over 10 and 100 Myr timescales calculated from the SFH. However, previous studies have shown that the SFR estimates can be biased because of the assumed parameterization of the SFH (Carnall et al. 2019). The FUV continuum is sensitive to the SFH over the past 100 Myr, and therefore one could expect that an SFR averaged over this timescale would be best correlated with the FUV–SFR relation from Kennicutt & Evans (2012). This is only true if the SFH does not vary significantly over 100 Myr. For the case that the SFH varies on timescales faster than this, then the SFR/$L_{\rm UV}$ is time dependent and varies by factors of several to an order of magnitude (Reddy et al. 2012). This is also true for SFHs that evolve exponentially in time (such as those assumed here; see Table 2). We therefore explore the impact of the SFH on the SED-measured SFRs here.

We compare the SFR averaged over 10 Myr ($\rm SFR_{C,10}$) and those averaged over 100 Myr ($\rm SFR_{C,100}$) to the dust-corrected FUV luminosity in Figure 9. These plots show that, while there is a strong correlation, the plots diverge from the FUV–SFR relation from Kennicutt & Evans (2012) at lower SFRs. Ultimately, we find that $\rm SFR_{C,10}$ shows a tighter relation to the FUV–SFR relation with a measured scatter of 0.11 dex. By contrast, the $\rm SFR_{C,100}$ values show a larger scatter of 0.215 dex. We therefore use the $\rm SFR_C$ values from CIGALE derived by averaging the SFH over the past 10 Myr. We do note, however, that there is an offset between the CIGALE $\rm SFR_C$ values and the $L_{\rm FUV}$ values at lower SFRs. We interpret this as a result of uncertainties in the assumed SFHs. This offset leads to the offsets seen in our relations in the main text (Figures 6 and 7), which we again attribute to the SFHs from CIGALE.

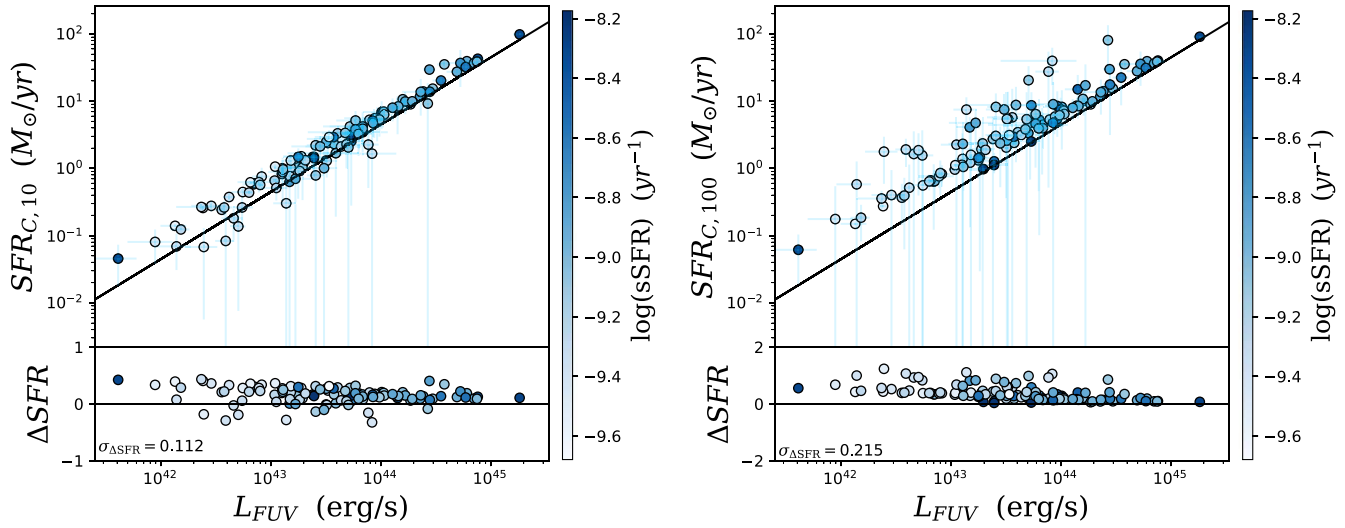

Figure 9. Left: CIGALE output SFRs measured by the average SFR over 10 (Myr, $\rm SFR_{C,10}$) from the SFH compared to dust-corrected FUV luminosity. Right: CIGALE output SFRs measured similarly to the left, but averaged over 100 (Myr, $\rm SFR_{C,100}$). Both figures are colored by sSFR in log scale and include the FUV–SFR relation from Kennicutt & Evans (2012) corrected to a Chabrier (2003) IMF shown in black. For each panel we measure the scatter about the FUV–SFR relation using $\Delta\rm SFR = \log(SFR_C, 10/100) - \log(SFR)$, where log(SFR) is the log of the FUV–SFR relation.

[27] https://svo.cab.inta-csic.es

Appendix B
The Relation between the 7.7 μm Luminosity and L_{770}

In this work we use the rest-frame mid-IR luminosity measured in the MIRI F770W bandpass. This bandpass includes the emission from the 7.7 μm PAH feature, which is the primary feature we use as a tracer of the SFR. However, the F770W bandpass includes the 7.7 μm PAH complex, the mid-IR continuum, and for some sources the Ar[II] and 8.6 μm PAH feature (Pagomenos et al. 2018). While we expect the 7.7 μm emission to dominate the total emission in this band based on observations of local star-forming galaxies (Chastenet et al. 2023; Whitcomb et al. 2023), here we consider how much of the rest-frame F770W luminosity stems from the PAH emission.

We compare our measurements of the PAH luminosity measured from the average flux in the rest-frame MIRI F770W bandpass (L_{770}) to the estimated 7.7 μm luminosity ($L_{7.7}$) from Kirkpatrick et al. (2023) in Figure 10. Kirkpatrick et al. independently measured the luminosity in the 7.7 μm PAH complex for galaxies in CEERS. Here, we cross-correlated the galaxies in our sample with those from Kirkpatrick et al., finding 86 galaxies common to both samples. Figure 10 compares the mid-IR luminosities from our work (L_{770}) with the 7.7 μm PAH luminosities estimated by Kirkpatrick et al. A full description of the estimation of $L_{7.7}$ from Kirkpatrick et al. can be found in Section 4.2 of their work (the method is the same as the measurement for $L_{6.2}$ in Section 4.2), but we will briefly describe it here. This work uses mid-IR spectroscopy to estimate the continuum contribution to the 7.7 μm feature with the 5MUSES sample that was observed with Spitzer/IRS.

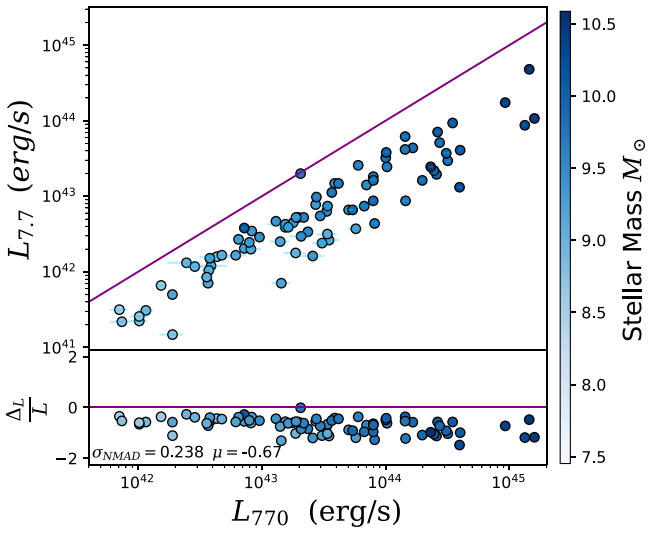

Figure 10. Top: the 7.7 μm luminosity estimated from Kirkpatrick et al. (2023) compared to L_{770}, with points colored by stellar mass estimated from CIGALE in log scale. The dark purple line shows the one-to-one relation. Bottom: measured scatter about the one-to-one relation, which is measured by $\Delta L = \log(L_{770}) - \log(L_{7.7})$. The data are colored by stellar mass in log scale. We argue that most of this offset is expected from the differences in the two methods (see text).

Kirkpatrick et al. selected 11 star-forming galaxies from the 5MUSES sample, which span redshifts 0.06–0.24 and $\log L_{\rm IR} = 10.79 - 11.63\, L_\odot$. Kirkpatrick et al. shifted the 5MUSES spectra into rest frame for sources that cover the 7.7 μm feature. They then calculated $L_{7.7}$(5MUSES) by fitting a line to the continuum at 7.2 and 8.2 μm to remove the continuum and then integrating the remaining luminosity. Kirkpatrick et al. also calculated a synthetic photometric point, L_ν, by convolving with the appropriate transmission curve. They used the ratio $L_{7.7}/L_\nu$ for the 5MUSES galaxies to estimate $L_{7.7}$ for the MIRI galaxies, which we use for this work.

We find that L_{770} is greater than $L_{7.7}$ by roughly 0.67 dex with a measured scatter of 0.24 dex. The reason for this offset is likely because of the difference in the methods. Here we take the average flux density in the rest-frame F770W bandpass, $\nu\langle f_\nu\rangle$, while Kirkpatrick et al. (2014) integrate over the continuum-subtracted line to get the total line flux, F. Assuming the continuum is negligible (see above), we can take the line flux to be $F = \langle f_\lambda\rangle \Delta\lambda$, where $\langle f_\lambda\rangle$ is the average flux density and $\Delta\lambda$ is the width of the F770W bandpass ($\Delta\lambda = 1.95$ μm). We further set $\nu\langle f_\nu\rangle = \lambda\langle f_\lambda\rangle$ and calculate the ratio. This leads to $\nu\langle f_\lambda\rangle/F \approx \lambda/\Delta\lambda = 7.7$ μm/1.95 μm, which is approximately a factor of 4, or (in logarithmic units) 0.6 dex. This is very nearly the observed offset (0.67 dex) and therefore reasonably accounts for the near-constant offset and tight scatter between the methods.

Appendix C
Binned PAH Luminosity Trends

We test if there is any dependence between the dust-corrected FUV luminosity and the 7.7 μm luminosity as a function of galaxy stellar mass and FUV attenuation (A(FUV)), using the values estimated by CIGALE. If rest-frame 7.7 μm luminosity directly traces the total SFR, we expect this ratio to be $\simeq$1.

To study any general trends in the data we measure the ratio of the dust-corrected UV luminosity to the 7.7 μm luminosity as a function of stellar mass and A(FUV). Figure 11 shows the results. At lower stellar masses ($<10^{9.4} M_\odot$), the galaxies in our sample have much higher ratios of FUV luminosity to the 7.7 μm luminosity, which reaches as high as a factor of 6. These galaxies tend to be optically thin ($A_V < 1$). For galaxies with higher stellar masses ($>10^{9.4} M_\odot$), the dust attenuation and the 7.7 μm luminosity increase with increasing stellar mass. In this case, we have already shown that the 7.7 μm luminosity scales with the total SFR (see Figure 5). The ratio of $L_{\rm FUV}/L_{770}$ dropping to unity for high stellar masses and high dust attenuation implies the existence of an additional source of PAH heating in these galaxies. This is expected as there exists heating from longer-lived stellar populations instead of from H II regions (Boselli et al. 2004). Therefore, it is most likely that these observed trends in our sample are caused by additional PAH heating (most likely from older stars) for galaxies at such high stellar mass.

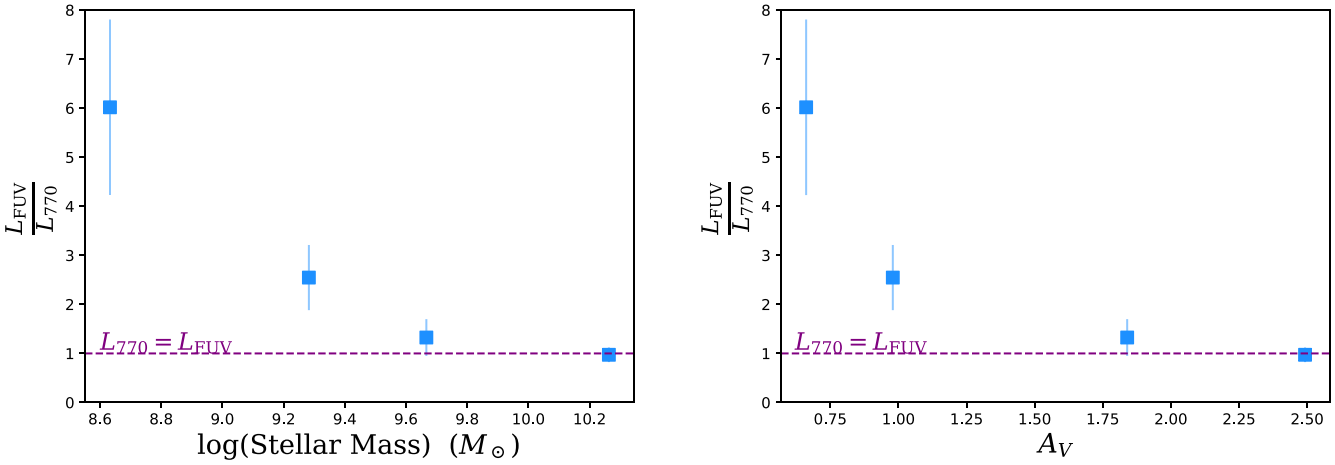

Figure 11. Binned ratio between dust-corrected FUV and PAH luminosity compared to the stellar mass in log scale (left) and FUV attenuation (A(FUV); right) . Both the stellar mass and A(FUV) are estimated from CIGALE as described in Section 4.1. The dark purple dashed line in both panels is the $L_{\rm FUV} = L_{770}$ line.

ORCID iDs

Kaila Ronayne https://orcid.org/0000-0001-5749-5452
Casey Papovich https://orcid.org/0000-0001-7503-8482
Guang Yang https://orcid.org/0000-0001-8835-7722
Lu Shen https://orcid.org/0000-0001-9495-7759
Mark Dickinson https://orcid.org/0000-0001-5414-5131
Robert Kennicutt https://orcid.org/0000-0001-5448-1821
Anahita Alavi https://orcid.org/0000-0002-8630-6435
Pablo Arrabal Haro https://orcid.org/0000-0002-7959-8783
Micaela B. Bagley https://orcid.org/0000-0002-9921-9218
Denis Burgarella https://orcid.org/0000-0002-4193-2539
Aurélien Le Bail https://orcid.org/0000-0002-9466-2763
Eric F. Bell https://orcid.org/0000-0002-5564-9873
Nikko J. Cleri https://orcid.org/0000-0001-7151-009X
Justin Cole https://orcid.org/0000-0002-6348-1900
Luca Costantin https://orcid.org/0000-0001-6820-0015
Alexander de la Vega https://orcid.org/0000-0002-6219-5558
Emanuele Daddi https://orcid.org/0000-0002-3331-9590
David Elbaz https://orcid.org/0000-0002-7631-647X
Steven L. Finkelstein https://orcid.org/0000-0001-8519-1130
Norman A. Grogin https://orcid.org/0000-0001-9440-8872
Benne W. Holwerda https://orcid.org/0000-0002-4884-6756
Jeyhan S. Kartaltepe https://orcid.org/0000-0001-9187-3605
Allison Kirkpatrick https://orcid.org/0000-0002-1306-1545
Anton M. Koekemoer https://orcid.org/0000-0002-6610-2048
Ray A. Lucas https://orcid.org/0000-0003-1581-7825
Benjamin Magnelli https://orcid.org/0000-0002-6777-6490
Bahram Mobasher https://orcid.org/0000-0001-5846-4404
Pablo G. Pérez-González https://orcid.org/0000-0003-4528-5639
Laura Prichard https://orcid.org/0000-0002-0604-654X
Marc Rafelski https://orcid.org/0000-0002-9946-4731
Giulia Rodighiero https://orcid.org/0000-0002-9415-2296
Ben Sunnquist https://orcid.org/0000-0003-3759-8707
Harry I. Teplitz https://orcid.org/0000-0002-7064-5424
Xin Wang https://orcid.org/0000-0002-9373-3865
Rogier A. Windhorst https://orcid.org/0000-0001-8156-6281
L. Y. Aaron Yung https://orcid.org/0000-0003-3466-035X

References

Acquaviva, V., Gawiser, E., & Guaita, L. 2012, in IAU Symp. 284, The Spectral Energy Distribution of Galaxies—SED 2011, ed. R. J. Tuffs & C. C. Popescu (Cambridge: Cambridge Univ. Press), 42
Astropy Collaboration, Price-Whelan, A. M., Lim, P. L., et al. 2022, ApJ, 935, 167
Astropy Collaboration, Price-Whelan, A. M., Sipőcz, B. M., et al. 2018, AJ, 156, 123
Astropy Collaboration, Robitaille, T. P., Tollerud, E. J., et al. 2013, A&A, 558, A33
Bagley, M. B., Finkelstein, S. L., Koekemoer, A. M., et al. 2023, ApJL, 946, L12
Battisti, A. J., Calzetti, D., Johnson, B. D., & Elbaz, D. 2015, ApJ, 800, 143
Bertin, E., & Arnouts, S. 1996, A&AS, 117, 393
Bolzonella, M., Miralles, J. M., & Pelló, R. 2000, A&A, 363, 476
Boquien, M., Burgarella, D., Roehlly, Y., et al. 2019, A&A, 622, A103
Boselli, A., Lequeux, J., & Gavazzi, G. 2004, A&A, 428, 409
Bruzual, G., & Charlot, S. 2003, MNRAS, 344, 1000
Bushouse, H., Eisenhamer, J., Dencheva, N., et al. 2023, JWST Calibration Pipeline, v1.10.2, Zenodo, doi:10.5281/zenodo.7829329
Calzetti, D., Armus, L., Bohlin, R. C., et al. 2000, ApJ, 533, 682
Calzetti, D., Kennicutt, R. C., Engelbracht, C. W., et al. 2007, ApJ, 666, 870
Calzetti, D., Kinney, A. L., & Storchi-Bergmann, T. 1994, ApJ, 429, 582
Carnall, A. C., Leja, J., Johnson, B. D., et al. 2019, ApJ, 873, 44
Chabrier, G. 2003, PASP, 115, 763
Chastenet, J., Sutter, J., Sandstrom, K., et al. 2023, ApJL, 944, L11
Cleri, N. J., Trump, J. R., Backhaus, B. E., et al. 2022, ApJ, 929, 3
Cluver, M. E., Jarrett, T. H., Hopkins, A. M., et al. 2014, ApJ, 782, 90
Coil, A. L., Davis, M., Madgwick, D. S., et al. 2004, ApJ, 609, 525
Cooper, M. C., Griffith, R. L., Newman, J. A., et al. 2012, MNRAS, 419, 3018
Dahlen, T., Mobasher, B., Faber, S. M., et al. 2013, ApJ, 775, 93
Dale, D. A., Boquien, M., Barnes, A. T., et al. 2023, ApJL, 944, L23
Davis, M., Guhathakurta, P., Konidaris, N. P., et al. 2007, ApJL, 660, L1
Donley, J. L., Koekemoer, A. M., Brusa, M., et al. 2012, ApJ, 748, 142
Draine, B. T., Aniano, G., Krause, O., et al. 2014, ApJ, 780, 172
Elbaz, D., Dickinson, M., Hwang, H. S., et al. 2011, A&A, 533, A119
Elbaz, D., Leiton, R., Nagar, N., et al. 2018, A&A, 616, A110
Engelbracht, C. W., Gordon, K. D., Rieke, G. H., et al. 2005, ApJL, 628, L29
Evans, A. S., Frayer, D. T., Charmandaris, V., et al. 2022, ApJL, 940, L8
Faber, S. 2011, The Cosmic Assembly Near-IR Deep Extragalactic Legacy Survey ("CANDELS"), STScI/MAST, doi:10.17909/T94S3X
Feigelson, E. D., & Babu, G. J. 1992, ApJ, 397, 55
Finkelstein, S., Bagley, M., & Yang, G. 2023, Data from The Cosmic Evolution Early Release Science Survey (CEERS), STScI/MAST, doi:10.17909/Z7P0-8481
Finkelstein, S. L., Dickinson, M., Ferguson, H. C., et al. 2017, The Cosmic Evolution Early Release Science (CEERS) Survey, JWST Proposal ID 1345
Fontana, A., D'Odorico, S., Poli, F., et al. 2000, AJ, 120, 2206
Fukugita, M., Ichikawa, T., Gunn, J. E., et al. 1996, AJ, 111, 1748
Gardner, J. P., Mather, J. C., Clampin, M., et al. 2006, SSRv, 123, 485
Gómez-Guijarro, C., Elbaz, D., Xiao, M., et al. 2022, A&A, 659, A196
Grogin, N. A., Kocevski, D. D., Faber, S. M., et al. 2011, ApJS, 197, 35

Hao, C.-N., Kennicutt, R. C., Johnson, B. D., et al. 2011, ApJ, 741, 124
Hernán-Caballero, A., Pérez-Fournon, I., Hatziminaoglou, E., et al. 2009, MNRAS, 395, 1695
Hirashita, H., Inoue, A. K., Kamaya, H., & Shibai, H. 2001, A&A, 366, 83
Houck, J. R., Weedman, D. W., Floc'h, E. L., & Hao, L. 2007, ApJ, 671, 323
Hunter, J. D. 2007, CSE, 9, 90
Ilbert, O., Arnouts, S., McCracken, H. J., et al. 2006, A&A, 457, 841
Jin, S., Daddi, E., Liu, D., et al. 2018, ApJ, 864, 56
Kelly, B. C. 2007, ApJ, 665, 1489
Kennicutt, R. C. 1998, ARA&A, 36, 189
Kennicutt, R. C., Jr., Calzetti, D., Walter, F., et al. 2007, ApJ, 671, 333
Kennicutt, R. C., & Evans, N. J. 2012, ARA&A, 50, 531
Kennicutt, R. C., Hao, C.-N., Calzetti, D., et al. 2009, ApJ, 703, 1672
Kirkpatrick, A., Pope, A., Aretxaga, I., et al. 2014, ApJ, 796, 135
Kirkpatrick, A., Yang, G., Le Bail, A., et al. 2023, ApJL, 959, L7
Koekemoer, A. M., Faber, S. M., Ferguson, H. C., et al. 2011, ApJS, 197, 36
Kriek, M., van Dokkum, P. G., Labbé, I., et al., 2018 FAST: Fitting and Assessment of Synthetic Templates, Astrophysics Source Code Library, ascl:1803.008
Le Bail, A., Daddi, E., Elbaz, D., et al. 2023, arXiv:2307.07599
Lee, S.-K., Ferguson, H. C., Somerville, R. S., Wiklind, T., & Giavalisco, M. 2010, ApJ, 725, 1644
Liu, D., Daddi, E., Dickinson, M., et al. 2018, ApJ, 853, 172
Madau, P., & Dickinson, M. 2014, ARA&A, 52, 415
McKinney, J., Pope, A., Armus, L., et al. 2020, ApJ, 892, 119
Merlin, E., Bourne, N., Castellano, M., et al. 2016, A&A, 595, A97
Mobasher, B., Dahlen, T., Ferguson, H. C., et al. 2015, ApJ, 808, 101
Newman, J. A., Cooper, M. C., Davis, M., et al. 2013, ApJS, 208, 5
Oke, J. B., & Gunn, J. E. 1983, ApJ, 266, 713
Pacifici, C., Iyer, K. G., Mobasher, B., et al. 2023, ApJ, 944, 141
Pagomenos, G. J. S., Bernard-Salas, J., & Pottasch, S. R. 2018, A&A, 615, A29
Papovich, C., Cole, J., Yang, G., et al. 2023, ApJL, 949, L18
Papovich, C., Rudnick, G., Rigby, J. R., et al. 2009, ApJ, 704, 1506
Perrin, M. D., Soummer, R., Elliott, E. M., Lallo, M. D., & Sivaramakrishnan, A. 2012, Proc. SPIE, 8442, 84423D
Pope, A., Chary, R.-R., Alexander, D. M., et al. 2008, ApJ, 675, 1171
Pope, A., Wagg, J., Frayer, D., et al. 2013, ApJ, 772, 92
Rafelski, M., Teplitz, H. I., Gardner, J. P., et al. 2015, AJ, 150, 31
Reback, J., jbrockmendel, M. W., et al. 2022, pandas-dev/pandas: Pandas v1.4.2, Zenodo, doi:10.5281/zenodo.6408044
Reddy, N. A., Pettini, M., Steidel, C. C., et al. 2012, ApJ, 754, 25
Rieke, G. H., Alonso-Herrero, A., Weiner, B. J., et al. 2009, ApJ, 692, 556
Rieke, G. H., Wright, G. S., Böker, T., et al. 2015, PASP, 127, 584
Rodrigo, C., & Solano, E. 2020, in XIV.0 Scientific Meeting of the Spanish Astronomical Society, 182
Rodrigo, C., Solano, E., & Bayo, A. 2012, SVO Filter Profile Service Version 1.0, IVOA Working Draft 15 October 2012
Senarath, M. R., Brown, M. J. I., Cluver, M. E., et al. 2018, ApJL, 869, L26
Shen, L., Papovich, C., Yang, G., et al. 2023, ApJ, 950, 7
Shipley, H. V., Papovich, C., Rieke, G. H., Brown, M. J. I., & Moustakas, J. 2016, ApJ, 818, 60
Smith, J. D. T., Draine, B. T., Dale, D. A., et al. 2007, ApJ, 656, 770
Stefanon, M., Yan, H., Mobasher, B., et al. 2017, ApJS, 229, 32
Takagi, T., Ohyama, Y., Goto, T., et al. 2010, A&A, 514, A5
Teplitz, H., Wang, X., Prichard, L., et al. 2022, Ultraviolet Imaging of the Cosmic Assembly Near-infrared Deep Extragalactic Legacy Survey Fields (UVCANDELS), STScI/MAST, doi:10.17909/8S31-F778
Teplitz, H. I., Rafelski, M., Kurczynski, P., et al. 2013, AJ, 146, 159
Virtanen, P., Gommers, R., Oliphant, T. E., et al. 2020, NatMe, 17, 261
Wang, X., Teplitz, H., Alavi, A., et al. 2020, AAS Meeting, 235, 426.03
Whitaker, K. E., Franx, M., Leja, J., et al. 2014, ApJ, 795, 104
Whitaker, K. E., Pope, A., Cybulski, R., et al. 2017, ApJ, 850, 208
Whitcomb, C. M., Sandstrom, K., & Smith, J.-D. T. 2023, RNAAS, 7, 38
Wiklind, T., Dickinson, M., Ferguson, H. C., et al. 2008, ApJ, 676, 781
Willner, S. P., Coil, A. L., Goss, W. M., et al. 2006, AJ, 132, 2159
Wright, G. S., Rieke, G. H., Glasse, A., et al. 2023, PASP, 135, 048003
Xie, Y., & Ho, L. C. 2019, ApJ, 884, 136
Xie, Y., & Ho, L. C. 2022, ApJ, 925, 218
Yang, G., Caputi, K. I., Papovich, C., et al. 2023a, ApJL, 950, L5
Yang, G., Papovich, C., Bagley, M., et al. 2023b, ApJL, 956, L12
Yang, G., Papovich, C., Bagley, M. B., et al. 2021, ApJ, 908, 144
Zahid, H. J., Kewley, L. J., & Bresolin, F. 2011, ApJ, 730, 137
Zhang, L., & Ho, L. C. 2023, ApJ, 943, 60